Available online at www.sciencedirect.com
SCIENCE DIRECT®
ELSEVIER
International Journal of Solids and Structures 43 (2006) 1131–1158
INTERNATIONAL JOURNAL OF SOLIDS and STRUCTURES
www.elsevier.com/locate/ijsolstr

An exact solution for the steady-state thermoelastic response of functionally graded orthotropic cylindrical shells

Jacob L. Pelletier, Senthil S. Vel *

University of Maine, Orono, ME 04469, USA

Received 3 November 2004; received in revised form 7 February 2005
Available online 1 September 2005

Abstract

We analyze the steady-state response of a functionally graded thick cylindrical shell subjected to thermal and mechanical loads. The functionally graded shell is simply supported at the edges and it is assumed to have an arbitrary variation of material properties in the radial direction. The three-dimensional steady-state heat conduction and thermoelasticity equations, simplified to the case of generalized plane strain deformations in the axial direction, are solved analytically. Suitable temperature and displacement functions that identically satisfy the boundary conditions at the simply supported edges are used to reduce the thermoelastic equilibrium equations to a set of coupled ordinary differential equations with variable coefficients, which are then solved by the power series method. In the present formulation, the cylindrical shell is assumed to be made of an orthotropic material, although the analytical solution is also valid for isotropic materials. Results are presented for two-constituent isotropic and fiber-reinforced functionally graded shells that have a smooth variation of material volume fractions, and/or in-plane fiber orientations, through the radial direction. The cylindrical shells are also analyzed using the Flügge and the Donnell shell theories. Displacements and stresses from the shell theories are compared with the three-dimensional exact solution to delineate the effects of transverse shear deformation, shell thickness and angular span.

Keywords: Inhomogeneous body; Fiber-reinforced material; Thermomechanical analysis; Three-dimensional elasticity solution; Shell theory

1. Introduction

Functionally graded materials (FGMs) are advanced composite materials that are engineered to have a smooth spatial variation of material properties. This is achieved by fabricating the composite material to

* Corresponding author. Tel.: +1 207 581 2777; fax: +1 207 581 2379.
E-mail address: senthil.vel@maine.edu (S.S. Vel).

0020-7683/$ - see front matter © 2005 Elsevier Ltd. All rights reserved.
doi:10.1016/j.ijsolstr.2005.03.079

have a gradual spatial variation of the constituent materials' relative volume fractions and microstructure, thus tailoring its material composition based on functional performance requirements (Miyamoto et al., 1999). FGMs offer great promise in applications where the operating conditions are severe, including spacecraft heat shields, heat exchanger tubes, plasma facings for fusion reactors, engine components, and high power electrical contacts or even magnets. For example, in a conventional thermal barrier coating for high temperature applications, a discrete layer of ceramic material is bonded to a metallic structure. However, the abrupt transition in material properties across the interface between distinct materials can cause large interlaminar stresses and lead to plastic deformation or cracking (Finot and Suresh, 1996). These adverse effects can be alleviated by functionally grading the material to have a smooth spatial variation of material composition, with ceramic-rich material placed at the high temperature locations and metal-rich material in regions where mechanical properties, such as toughness, need to be high.

Numerous studies have been performed to analyze the response of functionally graded plates. For example, Reddy (2000) has analyzed the static behavior of functionally graded rectangular plates based on a third-order shear deformation plate theory. Cheng and Batra (2000) and Reddy and Cheng (2001) have used the method of asymptotic expansion to study the three-dimensional thermoelastic deformations of functionally graded elliptic and rectangular plates, respectively. Vel and Batra (2002, 2003a,b) have presented exact three-dimensional solutions for the steady-state and quasi-static transient thermoelastic response of functionally graded thick plates with an arbitrary variation of material properties in the thickness direction. Qian et al. (2004) and Qian and Batra (2004) have obtained results for the steady-state and transient thermoelastic response of functionally graded plates using the meshless local Petrov–Galerkin method that compare well with the exact solution of Vel and Batra (2002, 2003a,b).

Research on functionally graded cylindrical shells has been primarily focussed on the analysis of thermal buckling and vibration using shells theories (e.g., Shahsiah and Eslami, 2003; Loy et al., 1999) and finite element formulations. However, in order to validate the kinematic assumptions and assess the accuracy of various shell theories and finite element formulations, it is important to obtain exact solutions to the three-dimensional heat conduction and thermoelasticity equations. The objective of this investigation is to provide an exact solution for simply supported functionally graded cylindrical shells subjected to steady-state thermal and mechanical loads. The governing partial differential equations of heat conduction and linear thermoelasticity, simplified to the case of generalized plane strain deformations in the axial direction, are exactly satisfied at every point of the cylindrical shell using a semi-inverse solution. The boundary conditions at the simply supported edges, the thermal and mechanical boundary conditions on the inner and outer surfaces of the shell and the continuity conditions at the interfaces between layers are also exactly satisfied. We assume that the shell is made of an orthotropic material with material properties that are functions of the radial coordinate and specifically consider two-phase isotropic or fiber-reinforced functionally graded cylindrical shells that have a smooth variation of volume fractions and in-plane fiber orientations through the radial direction. The effective material properties of the isotropic FGMs are determined in terms of the local volume fractions and material properties of the two isotropic phases by the self-consistent scheme (Hill, 1965). The effective material properties of the fiber-reinforced FGMs are estimated using the Composite Cylinder Assemblage model (Hashin, 1979). Results are presented for (a) isotropic Al/SiC FGM shells and (b) fiber-reinforced W/Cu FGM shells. Displacements and stresses from the shell theories are compared with the analytical solution for different length-to-thickness, length-to-radius and through-the-thickness variations of volume fractions and fiber orientations.

The paper is organized as follows. The coordinate system, three-dimensional equations of heat conduction and thermoelasticity, and boundary conditions are stated in Section 2. Exact solutions to the heat conduction and the generalized plane strain thermoelasticity problems are presented in Section 3. The Flügge and Donnell shell theories are formulated in Section 4 and the homogenization of material properties is discussed in Section 5. The analytical and shell theory results are compared for representative isotropic and fiber-reinforced shells in Section 6.

2. Problem formulation

We describe the geometry of a functionally graded cylindrical shell using a global, cylindrical coordinate system, with coordinates θ, x and r denoting the circumferential, axial and radial coordinate directions, respectively, as depicted in Fig. 1. The shell is assumed to be of infinite extent in the axial direction and composed of N functionally graded orthotropic layers, with each layer having a smooth variation of material properties in the radial direction. In this coordinate system, the functionally graded shell occupies the region $[0, \Theta]\times(-\infty, \infty)\times[r^{(0)}, r^{(N)}]$, where the inner surface and the outer surface of the shell are denoted by $r^{(0)}$ and $r^{(N)}$, respectively. A particular layer of the shell, denoted by the superscript (n), extends from $r^{(n-1)}$ to $r^{(n)}$ in the radial direction. In order to provide a more general shell solution that is also applicable to flat plates, we introduce a layerwise, local circumferential coordinate system with coordinate directions, $s^{(n)}$, $x^{(n)}$, and $z^{(n)}$ having the origin at the left edge ($\theta = 0$) of nth layer's midsurface as depicted in Fig. 1. The local circumferential coordinate system is related to the global cylindrical coordinate system through the transformations

$$s^{(n)} = R^{(n)}\theta, \quad z^{(n)} = r - R^{(n)}, \quad x^{(n)} = x, \tag{1}$$

where $s^{(n)}$ and $z^{(n)}$ are the local arc length and local thickness coordinate, respectively, with respect to the midsurface of the nth lamina. The midsurface radius, $R^{(n)}$, layer thickness, $h^{(n)}$, and midsurface circumferential length, $S^{(n)}$, of each layer are defined as

$$R^{(n)} = \frac{1}{2}(r^{(n)} + r^{(n-1)}), \quad h^{(n)} = r^{(n)} - r^{(n-1)}, \quad S^{(n)} = R^{(n)}\Theta. \tag{2}$$

In the local circumferential coordinate system, the nth layer occupies a region in $\mathbb{R}^3$ space denoted by $[0, S^{(n)}]\times(-\infty, \infty)\times[-h^{(n)}/2, h^{(n)}/2]$. Henceforth, we will drop the superscript (n) for convenience with the understanding that all material constants, geometric parameters and solution variables are for the nth layer unless the layer number is explicitly stated by a superscript.

Assuming that internal heat sources and body forces are absent, the three-dimensional steady-state heat conduction equation, expressed in terms of the local coordinates, is

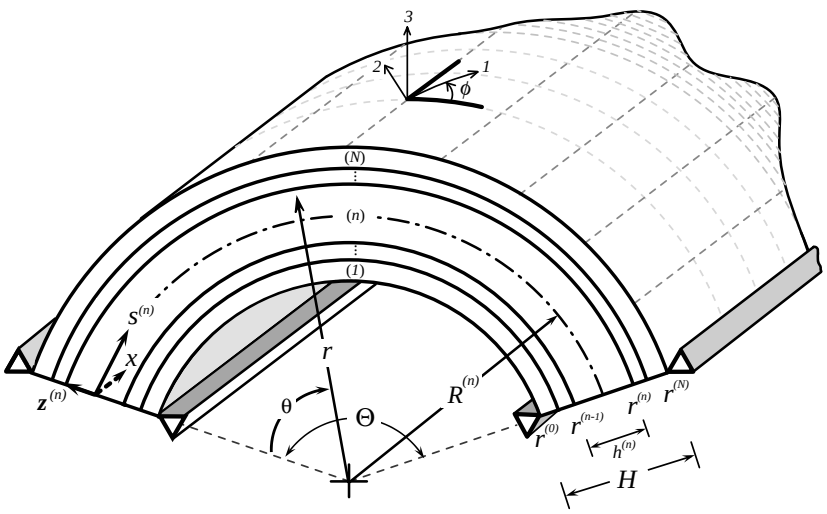

Fig. 1. Graphical depiction of a multilayer FGM cylindrical shell of infinite axial extent.

$$\frac{\partial q_r}{\partial z}+\frac{R}{R+z}\frac{\partial q_s}{\partial s}+\frac{\partial q_x}{\partial x}+\frac{q_r}{R+z}=0, \tag{3}$$

where q_r, q_s and q_x are the components of the heat flux vector. The corresponding three-dimensional mechanical equilibrium equations, are

$$\begin{aligned}
&\frac{\partial \sigma_{rr}}{\partial z}+\frac{R}{R+z}\frac{\partial \sigma_{rs}}{\partial s}+\frac{\partial \sigma_{rx}}{\partial x}+\frac{\sigma_{rr}-\sigma_{ss}}{R+z}=0,\\
&\frac{\partial \sigma_{rs}}{\partial z}+\frac{R}{R+z}\frac{\partial \sigma_{ss}}{\partial s}+\frac{\partial \sigma_{sx}}{\partial x}+\frac{2\sigma_{sr}}{R+z}=0,\\
&\frac{\partial \sigma_{rx}}{\partial z}+\frac{R}{R+z}\frac{\partial \sigma_{sx}}{\partial s}+\frac{\partial \sigma_{xx}}{\partial x}+\frac{\sigma_{rx}}{R+z}=0,
\end{aligned} \tag{4}$$

where σ_{rr}, σ_{ss}, σ_{xx}, σ_{rs}, σ_{rx} and σ_{sx} are the components of the Cauchy stress tensor in a circumferential coordinate system.

It is assumed that each layer of the functionally graded shell is made of a cylindrically orthotropic fiber-reinforced materials with principal material direction oriented at an angle ϕ to $\mathbf{e}_s$ on the cylindrical surface containing the base vectors $\mathbf{e}_x$ and $\mathbf{e}_s$. It is noted that the analytical solution presented here also applies to functionally graded isotropic shells. Fourier's law of heat conduction, which relates the heat flux to the temperature gradient, is

$$\begin{Bmatrix} q_s \\ q_x \\ q_r \end{Bmatrix} = -\begin{bmatrix} \kappa_{11} & \kappa_{12} & 0 \\ \kappa_{12} & \kappa_{22} & 0 \\ 0 & 0 & \kappa_{33} \end{bmatrix} \begin{Bmatrix} \dfrac{R}{R+z}\dfrac{\partial T}{\partial s} \\ \dfrac{\partial T}{\partial x} \\ \dfrac{\partial T}{\partial z} \end{Bmatrix}, \tag{5}$$

where T is the change in temperature of a material particle from that in the stress-free reference configuration and κ_{ij} are the thermal conductivities. The mechanical constitutive equations, which relate the stresses to the strains and change in temperature, are

$$\begin{Bmatrix} \sigma_{ss} \\ \sigma_{xx} \\ \sigma_{rr} \\ \sigma_{rx} \\ \sigma_{rs} \\ \sigma_{sx} \end{Bmatrix} = \begin{bmatrix} C_{11} & C_{12} & C_{13} & 0 & 0 & C_{16} \\ C_{12} & C_{22} & C_{23} & 0 & 0 & C_{26} \\ C_{13} & C_{23} & C_{33} & 0 & 0 & C_{36} \\ 0 & 0 & 0 & C_{44} & C_{45} & 0 \\ 0 & 0 & 0 & C_{45} & C_{55} & 0 \\ C_{16} & C_{26} & C_{36} & 0 & 0 & C_{66} \end{bmatrix} \begin{Bmatrix} \varepsilon_{ss} \\ \varepsilon_{xx} \\ \varepsilon_{rr} \\ 2\varepsilon_{rx} \\ 2\varepsilon_{rs} \\ 2\varepsilon_{sx} \end{Bmatrix} - \begin{Bmatrix} \beta_{11} \\ \beta_{22} \\ \beta_{33} \\ 0 \\ 0 \\ \beta_{12} \end{Bmatrix} T, \tag{6}$$

where C_{ij} are the elastic stiffnesses, ε_{ss}, ε_{xx}, ε_{rr}, ε_{rx}, ε_{rs} and ε_{sx} are the components of the infinitesimal strain tensor in a cylindrical coordinate system and β_{ij} are the stress moduli that are related to the thermal expansion coefficients α_{ij} as follows:

$$\begin{Bmatrix} \beta_{11} \\ \beta_{22} \\ \beta_{33} \\ \beta_{12} \end{Bmatrix} = \begin{Bmatrix} C_{11}\alpha_{11}+C_{12}\alpha_{22}+C_{13}\alpha_{33}+2C_{16}\alpha_{12} \\ C_{12}\alpha_{11}+C_{22}\alpha_{22}+C_{23}\alpha_{33}+2C_{26}\alpha_{12} \\ C_{13}\alpha_{11}+C_{23}\alpha_{22}+C_{33}\alpha_{33}+2C_{36}\alpha_{12} \\ C_{16}\alpha_{11}+C_{26}\alpha_{22}+C_{36}\alpha_{33}+2C_{66}\alpha_{12} \end{Bmatrix}. \tag{7}$$

Since the shell is graded in the radial direction, the material properties κ_{ij}, C_{ij} and α_{ij} are functions of the radial coordinate, r. Employing our circumferential coordinate system, the infinitesimal strain tensor is related to the displacements as follows:

$$\varepsilon_{ss} = \frac{R}{R+z}\frac{\partial u_s}{\partial s} + \frac{u_r}{R+z}, \quad \varepsilon_{xx} = \frac{\partial u_x}{\partial x}, \quad \varepsilon_{rr} = \frac{\partial u_r}{\partial z},$$
$$\varepsilon_{xr} = \frac{1}{2}\left(\frac{\partial u_x}{\partial z} + \frac{\partial u_r}{\partial x}\right), \quad \varepsilon_{sr} = \frac{1}{2}\left(\frac{R}{R+z}\frac{\partial u_r}{\partial s} + \frac{\partial u_s}{\partial z} - \frac{u_s}{R+z}\right), \tag{8}$$
$$\varepsilon_{sx} = \frac{1}{2}\left(\frac{\partial u_s}{\partial x} + \frac{R}{R+z}\frac{\partial u_x}{\partial s}\right).$$

We note that since the shell is viewed as a three-dimensional body, it is necessary to prescribe either a displacement or traction component in each coordinate direction at every point on the boundary. We assume that the shell is simply supported and maintained at the constant ambient reference temperature at the edges and prescribe the following mixed boundary conditions:

$$u_r = 0, \quad \sigma_{ss} = \sigma_{sx} = 0, \quad T = 0 \quad \text{at } s = 0, S. \tag{9}$$

Additional mechanical boundary conditions are imposed at the inner and outer surfaces of the shell by prescribing either displacement or corresponding traction components, u_r or σ_{rr}, u_s or σ_{sr}, and u_x or σ_{xr}, which are assumed to be independent of the axial coordinate. Although it is possible to prescribe the displacements, it is customary to prescribe only tractions on the inner and outer surfaces of the shell. Since the applied loads can be expanded as Fourier series, it is sufficient to solve the problem of a shell subjected to the following sinusoidal loads:

$$\begin{aligned}
&\sigma_{rr}^{(1)} = p_r^- \sin\frac{k\pi s}{S}, \quad \sigma_{sr}^{(1)} = p_s^- \cos\frac{k\pi s}{S}, \quad \sigma_{xr}^{(1)} = p_x^- \cos\frac{k\pi s}{S} \quad \text{at } z^{(1)} = -h^{(1)}/2,\\
&\sigma_{rr}^{(N)} = p_r^+ \sin\frac{k\pi s}{S}, \quad \sigma_{sr}^{(N)} = p_s^+ \cos\frac{k\pi s}{S}, \quad \sigma_{xr}^{(N)} = p_x^+ \cos\frac{k\pi s}{S} \quad \text{at } z^{(N)} = h^{(N)}/2,
\end{aligned} \tag{10}$$

where the superscripts (1) and (N) denote the layer numbers, k is a positive integer that specifies the harmonic of the sinusoidal distributed load and constants p_r^-, p_s^-, p_x^- and p_r^+, p_s^+, p_x^+ specify the corresponding amplitudes on the inner and outer surfaces, respectively. Similarly, the thermal boundary conditions on these surfaces are specified as

$$\begin{aligned}
&\vartheta^- T^{(1)} + \xi^- q_r^{(1)} = \chi^- \sin\frac{k\pi s}{S},\\
&\vartheta^+ T^{(N)} + \xi^+ q_r^{(N)} = \chi^+ \sin\frac{k\pi s}{S},
\end{aligned} \tag{11}$$

where χ^- and χ^+ are prescribed constants, and various thermal boundary conditions, corresponding to either prescribed temperatures or heat fluxes or exposure to ambient temperature through boundary convection, are specified by appropriately choosing the constants ϑ^-, ξ^-, ϑ^+ and ξ^+. The functionally graded layers are assumed to be in ideal thermal contact and perfectly bonded together and the following thermal and mechanical continuity conditions are assumed at the interfaces $r = r^{(n)}$ for $n = 1, \ldots, N-1$, (Nowinski, 1978; Hyer and Rousseau, 1987)

$$[[T]] = 0, \quad [[q_r]] = 0, \quad [[u_r]] = [[u_s]] = [[u_x]] = 0, \quad [[\sigma_{rr}]] = [[\sigma_{sr}]] = [[\sigma_{xr}]] = 0, \tag{12}$$

where $[[g]]$ denotes the jump in the value of g across the interface.

The steady-state formulation leads to a one way coupling of the governing equations. Specifically, the temperature field affects the mechanical response of the shell, but the mechanical response has no influence on the temperature field. First, the temperature field is obtained by solving the heat conduction equations (3), (5) with the pertinent boundary conditions (9), (11) and the continuity conditions (12) at the interfaces. Subsequently, the displacements are obtained by solving for shell equilibrium, (4), through the constitutive equations (6), the pertinent boundary conditions (9), (10) and the continuity conditions (12) at the

interfaces. We assume that material properties of each layer of the functionally graded shell are analytic functions of the radial coordinate z, and, thus, can be represented by a Taylor series expansion about its midsurface as

$$[\kappa_{ij}, C_{ij}, \beta_{ij}] = \sum_{\alpha=0}^{\infty} \left[\kappa_{ij}^{(\alpha)}, C_{ij}^{(\alpha)}, \beta_{ij}^{(\alpha)}\right] z^a. \tag{13}$$

This assumption, however, is not a significant limitation on the applicability of the analytical solution. Functionally graded shells that exhibit discontinuous or non-smooth material properties at a finite number of radial locations, can be analyzed by introducing fictitious interfaces at those locations. Thus, the formulation enables us to analyze shells with abrupt changes in volume fractions of the constituent phases and/or discontinuous material microstructure in the radial direction.

3. Analytical solution

Since the applied loads and material properties are independent of x and the body is of infinite extent in the axial direction, we postulate that the temperature change, T, and displacement vector, $\mathbf{u}$, are functions of r and s only. Thus, deformations of the functionally graded shell correspond to a generalized plane strain state of deformation. It is noted that due to the generalized plane strain assumption, the out of plane displacements $u_x = u_x(s, z)$ in the axial direction may be non-zero, as may be the case for orthotropic layers with principal material directions oriented at an angle to the geometric axes.

3.1. Temperature field

We seek a semi-inverse solution to the heat conduction problem by assuming the following form for the temperature field

$$T = \eta(z) \sin ps, \tag{14}$$

where $p = k\pi/S$. The assumed form of the temperature field identically satisfies the homogeneous boundary conditions (9) for the temperature at the edges. Substitution for T from (14) into (5) yields the components of the heat flux vector,

$$\begin{aligned} q_r &= -\kappa_{33}\eta' \sin ps, \\ q_s &= -\frac{pR}{R+z}\kappa_{11}\eta \cos ps, \\ q_x &= -\frac{pR}{R+z}\kappa_{12}\eta \cos ps, \end{aligned} \tag{15}$$

where a prime denotes derivative with respect to z. Substitution of (15) into (3) and requiring that the resulting equation hold for arbitrary s, results in the following second-order ordinary differential equation with variable coefficients

$$\kappa_{33}\eta'' + \kappa_{33}'\eta' + \left(\frac{1}{R+z}\right)\kappa_{33}\eta' - \left(\frac{R}{R+z}\right)^2 p^2\kappa_{11}\eta = 0. \tag{16}$$

We assume a solution for $\eta(z)$ in the form of a power series

$$\eta(z) = \sum_{\beta=0}^{\infty} \eta^{(\beta)} z^{\beta}. \tag{17}$$

Furthermore, we utilize the following Taylor series expansions to facilitate the solution process

$$\left[\left(\frac{1}{R+z}\right),\left(\frac{R}{R+z}\right),\left(\frac{R}{R+z}\right)^2\right]=\sum_{\alpha=0}^{\infty}[\phi^{(\alpha)},\varsigma^{(\alpha)},\psi^{(\alpha)}]z^{\alpha}, \tag{18}$$

where the series coefficients are defined as

$$\phi^{(\alpha)}=\frac{(-1)^{\alpha}}{R^{\alpha+1}},\quad \varsigma^{(\alpha)}=\frac{(-1)^{\alpha}}{R^{\alpha}},\quad \psi^{(\alpha)}=\frac{(\alpha+1)(-1)^{\alpha}}{R^{\alpha}}.$$

Substitution of (13), (17) and (18) into (16), multiplying the infinite series, appropriately shifting the index of summation, and equating each power of z to zero, results in the following recurrence relation

$$\sum_{\beta=0}^{\alpha}\left\{(\alpha-\beta+1)(\alpha-\beta+2)\kappa_{33}^{(\beta)}\eta^{(\alpha-\beta+2)}+(\beta+1)(\alpha-\beta+1)\kappa_{33}^{(\beta+1)}\eta^{(\alpha-\beta+1)}+\sum_{\gamma}^{\alpha-\beta}\left[(\alpha-\beta-\gamma+1)\phi^{(\beta)}\kappa_{33}^{(\gamma)}\eta^{(a-\beta-\gamma+1)}-\psi^{(\beta)}p^2\kappa_{11}^{(\gamma)}\eta^{(\alpha-\beta-\gamma)}\right]\right\}=0, \tag{19}$$

which has to hold true for every $\alpha=0,1,2,\ldots$ The recurrence relation (19) is evaluated successively for $\alpha=0,1,\ldots$ to obtain the coefficients $\eta^{(\alpha+2)}$ in terms of two constants, $\eta^{(0)}$ and $\eta^{(1)}$. The power series coefficients $\eta^{(k)}$ are then inserted into (17) to obtain $\eta(z)$, and hence the change in temperature T and heat flux q through (14) and (15), in terms of two constants, namely $\eta^{(0)}$ and $\eta^{(1)}$. For an N-layer shell, the power series solution procedure results in $2N$ constants. The constants are determined by satisfying the thermal boundary conditions (11) on the top and bottom surfaces of the shell and the thermal continuity conditions (12) at each of the $N-1$ interfaces. The resulting system of $2N$ linear algebraic equations for the $2N$ unknowns is readily solved to obtain $\eta^{(0)}$ and $\eta^{(1)}$ for each layer. The series coefficients $\eta^{(\beta)}$, thus obtained, are reinserted into (17), (14) and (15) to yield the temperature and heat flux components for each layer.

3.2. Displacement field

With the temperature field established, we seek a semi-inverse solution for the displacement field by assuming that

$$[u_s,u_x]=[U_s(z),U_x(z)]\cos ps,\quad u_r=U_r(z)\sin ps. \tag{20}$$

As in the case of the thermal solution, simply supported boundary conditions at the edges of a layer are identically satisfied by the assumed displacement field. We insert these assumed displacement forms into the strain-displacement relations (8) to obtain

$$\begin{aligned}
&\varepsilon_{ss}=\left(-\frac{Rp}{R+z}U_s+\frac{U_r}{R+z}\right)\sin ps,\quad \varepsilon_{xx}=0,\quad \varepsilon_{rr}=U_r'\sin ps,\\
&\varepsilon_{xr}=\frac{1}{2}U_x'\cos ps,\quad \varepsilon_{sr}=\frac{1}{2}\left(\frac{Rp}{R+z}U_r+U_s'-\frac{U_s}{R+z}\right)\cos ps,\\
&\varepsilon_{sx}=-\frac{1}{2}\left(\frac{Rp}{R+z}U_x\right)\sin ps,
\end{aligned} \tag{21}$$

The stress components, which are obtained from the strains (21) and the constitutive equations (6), are substituted into the equilibrium equations (4), to yield three coupled ordinary differential equations with variable coefficients

$$
\begin{aligned}
&C_{33}U_r'' + C_{33}'U_r' - (\beta_{33}\eta' + \beta_{33}'\eta) + \left(\frac{1}{R+z}\right)^2((-C_{11} - p^2R^2C_{55})U_r + pR(C_{11} + C_{55})U_s \\
&\quad + pRC_{16}U_x)) + \left(\frac{1}{R+z}\right)((\beta_{11} - \beta_{33})\eta + C_{13}'U_r - pRC_{13}'U_s - pRC_{36}'U_x + C_{33}U_r' \\
&\quad - pR(C_{13} + C_{55})U_s' - pR(C_{36} + C_{45})U_x') = 0, \\
&C_{55}U_s'' + C_{55}'U_s' + C_{45}U_x'' + C_{45}'U_x' + \left(\frac{1}{R+z}\right)^2(pR(C_{11} + C_{55})U_r - (p^2R^2C_{11} + C_{55})U_s \\
&\quad - p^2R^2C_{16}U_x) + \left(\frac{1}{R+z}\right)(-pR\beta_{11}\eta + pRC_{55}'U_r - C_{55}'U_s + pR(C_{13} + C_{55})U_r' + C_{55}U_s' + 2C_{45}U_x') = 0, \\
&C_{45}U_s'' + C_{45}'U_s' + C_{44}U_x'' + C_{44}'U_x' + \left(\frac{1}{R+z}\right)^2(pRC_{16}U_r - p^2R^2C_{16}U_s - p^2R^2C_{66}U_x) \\
&\quad + \left(\frac{1}{R+z}\right)(-pR\beta_{12}\eta + pRC_{45}'U_r - C_{45}'U_s + pR(C_{36} + C_{45})U_r' + C_{44}U_x') = 0.
\end{aligned}
\tag{22}
$$

A solution to the system of ordinary differential equations (22) is obtained by assuming a power series representation for $U_r(z)$, $U_s(z)$, $U_x(z)$,

$$
[U_r(z), U_s(z), U_x(z)] = \sum_{\beta=0}^{\infty} \left[U_r^{(\beta)}, U_s^{(\beta)}, U_x^{(\beta)}\right] z^{\beta}. \tag{23}
$$

The power series (23), the Taylor series expansions (13) and (18), and the previously computed power series solution for the temperature field (17), are substituted into the system of ordinary differential equations (22) to yield the following recurrence relations:

$$
\begin{aligned}
\text{(i)}\quad &\sum_{\beta=0}^{\alpha}\Bigg\{(\alpha-\beta+1)(\alpha-\beta+2)C_{33}^{(\beta)}U_r^{(\alpha-\beta+2)} + (\beta+1)(\alpha-\beta+1)C_{33}^{(\beta+1)}U_r^{(\alpha-\beta+1)} \\
&\quad - (\alpha-\beta+1)\beta_{33}^{(\beta)}\eta^{(\alpha-\beta+1)} - (\beta+1)\beta_{33}^{(\beta+1)}\eta^{(\alpha-\beta)} \\
&\quad + \sum_{\gamma=0}^{\alpha-\beta}\Bigg[\psi^{(\beta)}\Bigg[\left(-\frac{1}{R^2}C_{11}^{(\gamma)} - p^2C_{55}^{(\gamma)}\right)U_r^{(\alpha-\beta-\gamma)} + \frac{p}{R}\left(C_{11}^{(\gamma)} + C_{55}^{(\gamma)}\right)U_s^{(\alpha-\beta-\gamma)} + \frac{p}{R}C_{16}^{(\gamma)}U_x^{(\alpha-\beta-\gamma)}\Bigg] \\
&\quad + \phi^{(\beta)}\Bigg[\left(\beta_{11}^{(\gamma)} - \beta_{33}^{(\gamma)}\right)\eta^{(\alpha-\beta-\gamma)} + (\gamma+1)C_{13}^{(\gamma+1)}U_r^{(\alpha-\beta-\gamma)} + (\alpha-\beta-\gamma+1)C_{33}^{(\gamma)}U_r^{(\alpha-\beta-\gamma+1)}\Bigg] \\
&\quad + \varsigma^{(\beta)}\Bigg[-p(\gamma+1)C_{13}^{(\gamma+1)}U_s^{(\alpha-\beta-\gamma)} - p(\gamma+1)C_{36}^{(\gamma+1)}U_x^{(\alpha-\beta-\gamma)} - p(\alpha-\beta-\gamma+1)(C_{13}^{(\gamma)} + C_{55}^{(\gamma)})U_s^{(\alpha-\beta-\gamma+1)} \\
&\quad - p(\alpha-\beta-\gamma+1)\left(C_{36}^{(\gamma)} + C_{45}^{(\gamma)}\right)U_x^{(\alpha-\beta-\gamma+1)}\Bigg]\Bigg]\Bigg\} = 0, \\
\text{(ii)}\quad &\sum_{\beta=0}^{\alpha}\Bigg\{(\alpha-\beta+1)(\alpha-\beta+2)C_{55}^{(\beta)}U_s^{(\alpha-\beta+2)} + (\beta+1)(\alpha-\beta+1)C_{55}^{(\beta+1)}U_s^{(\alpha-\beta+1)} \\
&\quad + (\alpha-\beta+1)(\alpha-\beta+2)C_{45}^{(\beta)}U_x^{(\alpha-\beta+2)} + (\beta+1)(\alpha-\beta+1)C_{45}^{(\beta+1)}U_x^{(\alpha-\beta+1)} \\
&\quad + \sum_{\gamma=0}^{\alpha-\beta}\Bigg[\psi^{(\beta)}\Bigg[\frac{p}{R}\left(C_{11}^{(\gamma)} + C_{55}^{(\gamma)}\right)U_r^{(\alpha-\beta-\gamma)} - \left(p^2C_{11}^{(\gamma)} + C_{55}^{(\gamma)}\right)U_s^{(\alpha-\beta-\gamma)} - p^2C_{16}^{(\gamma)}U_x^{(\alpha-\beta-\gamma)}\Bigg] \\
&\quad + \varsigma^{(\beta)}\Bigg[-p\beta_{11}^{(\gamma)}\eta^{(\alpha-\beta-\gamma)} + p(\gamma+1)C_{55}^{(\gamma+1)}U_r^{(\alpha-\beta-\gamma)} + p(\alpha-\beta-\gamma+1)\left(C_{13}^{(\gamma)} + C_{55}^{(\gamma)}\right)U_r^{(\alpha-\beta-\gamma+1)}\Bigg] \\
&\quad + \phi^{(\beta)}\Bigg[-(\gamma+1)C_{55}^{(\gamma+1)}U_s^{(\alpha-\beta-\gamma)} + (\alpha-\beta-\gamma+1)C_{55}^{(\gamma)}U_s^{(\alpha-\beta-\gamma+1)} \\
&\quad + 2(\alpha-\beta-\gamma+1)C_{45}^{(\gamma)}U_x^{(\alpha-\beta-\gamma+1)}\Bigg]\Bigg]\Bigg\} = 0,
\end{aligned}
$$

$$\text{(iii)}\quad \sum_{\beta=0}^{\alpha}\Bigg\{(\alpha-\beta+1)(\alpha-\beta+2)C_{45}^{(\beta)}U_s^{(\alpha-\beta+2)}+(\beta+1)(\alpha-\beta+1)C_{45}^{(\beta+1)}U_s^{(\alpha-\beta+1)}$$
$$+(\alpha-\beta+1)(\alpha-\beta+2)C_{44}^{(\beta)}U_x^{(\alpha-\beta+2)}+(\beta+1)(\alpha-\beta+1)C_{44}^{(\beta+1)}U_x^{(\alpha-\beta+1)}$$
$$+\sum_{\gamma=0}^{\alpha-\beta}\left[\psi^{(\beta)}\left[\frac{p}{R}C_{16}^{(\gamma)}U_r^{(\alpha-\beta-\gamma)}-p^2C_{16}^{(\gamma)}U_s^{(\alpha-\beta-\gamma)}-p^2C_{66}^{(\gamma)}U_x^{(\alpha-\beta-\gamma)}\right]\right.$$
$$+\varsigma^{(\beta)}\left[-p\beta_{12}^{(\gamma)}\eta^{(\alpha-\beta-\gamma)}+p(\gamma+1)C_{45}^{(\gamma+1)}U_r^{(\alpha-\beta-\gamma)}+p(\alpha-\beta-\gamma+1)\left(C_{36}^{(\gamma)}+C_{45}^{(\gamma)}\right)U_r^{(\alpha-\beta-\gamma+1)}\right]$$
$$\left.+\phi^{(\beta)}\left[-(\gamma+1)C_{45}^{(\gamma+1)}U_s^{(\alpha-\beta-\gamma)}+(\alpha-\beta-\gamma+1)C_{44}^{(\gamma)}U_x^{(\alpha-\beta-\gamma+1)}\right]\right]\Bigg\}=0. \tag{24}$$

which have to hold true for every $\alpha = 0, 1, 2, \ldots$ The recurrence relations (24) are evaluated successively for $\alpha = 0, 1, \ldots$ to obtain three simultaneous equations, which are solved to obtain $U_s^{(\alpha+2)}, U_x^{(\alpha+2)}$ and $U_r^{(\alpha+2)}$ in terms of six unknown constants $U_s^{(0)}, U_x^{(0)}, U_r^{(0)}, U_s^{(1)}, U_x^{(1)}$ and $U_r^{(1)}$. The power series coefficients $U_s^{(k)}, U_x^{(k)}$ and $U_r^{(k)}$ are inserted into (23) to obtain $U_s(z)$, $U_x(z)$ and $U_r(z)$, and hence the components of the displacement field u_s, u_x and u_r and strain field using (20) and (21), in terms of six constants, namely $U_s^{(0)}, U_x^{(0)}, U_r^{(0)}, U_s^{(1)}, U_x^{(1)}$ and $U_r^{(1)}$. For an N-layer shell, the power series solution procedure results in $6N$ constants. The constants are determined by satisfying the traction boundary conditions (10) on the top and bottom surfaces of the shell and the mechanical continuity conditions (12) at each of the $N-1$ interfaces. The resulting system of $6N$ linear algebraic equations for the $6N$ unknowns is readily solved to obtain $U_s^{(0)}, U_x^{(0)}, U_r^{(0)}, U_s^{(1)}, U_x^{(1)}$ and $U_r^{(1)}$ for each layer. The solution for the series coefficients, $U_s^{(k)}, U_x^{(k)}$ and $U_r^{(k)}$, are reinserted into (23), (20), (21) and (6) to yield the displacements, strains and stresses corresponding to each layer.

4. Classical and shear deformable shell theories

In this section, we present a concise formulation of the Flügge shell theory (Flügge, 1973) by integrating the three-dimensional equilibrium equations (4) through the thickness of the shell. The resulting equilibrium equations for the shell are stated in terms of force and moment resultants. The kinematic assumptions, which are based on either the classical or the first-order shear deformation theories, are presented in unified form using tracers. The Donnell shallow (thin) shell theory is obtained from the Flügge shell theory by assuming that the thickness of the shell is much smaller than the midsurface radius.

4.1. Flügge shell theory

The Flügge shell theory is formulated by introducing a global circumferential coordinate system denoted by z, s and x, where $z = 0$ corresponds to the global shell midsurface. The circumferential and thickness coordinate are related to the cylindrical coordinates by $s = R\theta$, $z = r - R$ where $R = (r^{(0)} + r^{(N)})/2$. The cylindrical shell occupies the region $[0, S]\times[L, -L]\times[-H/2, H/2]$ as depicted in Fig. 2, where $S = R\Theta$ and $H = r^{(N)} - r^{(0)}$. The force and moment resultant that act on a shell element are defined as the force and moments per unit *per unit length* of the shell's midsurface. The force and moment resultants, which are obtained by integrating the stresses acting on differential area elements of a shell element, have the following definitions

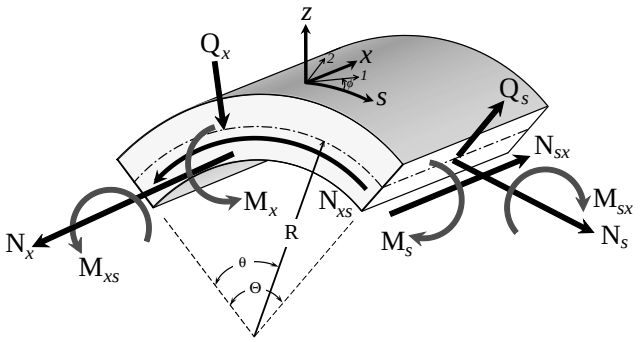

Fig. 2. Graphical depiction of a finite length monolayer FGM cylindrical shell including stress and moment resultants as required by shell theory.

$$\{N_s, N_{sx}, N_x, N_{xs}\} = \int_{-H/2}^{H/2} \left\{\sigma_{ss}, \sigma_{sx}, \left(1+\frac{z}{R}\right)\sigma_{xx}, \left(1+\frac{z}{R}\right)\sigma_{xs}\right\} \mathrm{d}z, \tag{25}$$

$$\{M_s, M_{sx}, M_x, M_{xs}\} = \int_{-H/2}^{H/2} \left\{\sigma_{ss}, \sigma_{sx}, \left(1+\frac{z}{R}\right)\sigma_{xx}, \left(1+\frac{z}{R}\right)\sigma_{xs}\right\} z \,\mathrm{d}z, \tag{26}$$

$$\{Q_s, Q_x\} = \int_{-H/2}^{H/2} \left\{\sigma_{sr}, \left(1+\frac{z}{R}\right)\sigma_{xr}\right\} \mathrm{d}z. \tag{27}$$

The equilibrium equations of the shell are systematically obtained by integrating the pointwise three-dimensional equilibrium equations in the radial direction. Eq. $(4)_1$ is multiplied by $(R+z)/R$ and integrated through the thickness of the shell

$$\int_{-H/2}^{H/2} \left\{\left(1+\frac{z}{R}\right)\frac{\partial \sigma_{rr}}{\partial z} + \frac{\sigma_{rr}}{R} + \frac{\partial \sigma_{sr}}{\partial s} + \left(1+\frac{z}{R}\right)\frac{\partial \sigma_{xr}}{\partial x} - \frac{\sigma_{ss}}{R}\right\} = 0,$$

$$\int_{-H/2}^{H/2} \left\{\frac{\partial \sigma_{rr}}{\partial z} + \frac{1}{R}\frac{\partial (z\sigma_{rr})}{\partial z} + \frac{\partial \sigma_{sr}}{\partial s} + \left(1+\frac{z}{R}\right)\frac{\partial \sigma_{xr}}{\partial x} - \frac{\sigma_{ss}}{R}\right\} = 0,$$

to yield the following shell equilibrium equation

$$\frac{\partial Q_s}{\partial s} + \frac{\partial Q_x}{\partial x} - \frac{N_s}{R} + \mathscr{P}_r = 0, \tag{28}$$

where $\mathscr{P}_r$ is the applied radial load per unit midsurface area due to the radial component of the tractions on the top and bottom surfaces

$$\mathscr{P}_r = \left(1+\frac{H}{2R}\right)\sigma_{rr}\left(s, x, \frac{H}{2}\right) - \left(1-\frac{H}{2R}\right)\sigma_{rr}\left(s, x, -\frac{H}{2}\right). \tag{29}$$

Similarly, $(4)_2$ and $(4)_3$ are multiplied by $(R+z)/R$ and integrated through the thickness of the shell to yield

$$\frac{\partial N_s}{\partial s} + \frac{\partial N_{xs}}{\partial x} + \frac{Q_s}{R} + \mathscr{P}_s = 0, \tag{30}$$

$$\frac{\partial N_{sx}}{\partial s} + \frac{\partial N_x}{\partial x} + \mathscr{P}_x = 0, \tag{31}$$

where $\mathscr{P}_s$ and $\mathscr{P}_x$ are the applied circumferential and axial shear load, respectively, per unit midsurface area due to the tractions on the top and bottom surfaces

$$\begin{aligned}\mathscr{P}_s &= \left(1+\frac{H}{2R}\right)\sigma_{rs}\left(s,x,\frac{H}{2}\right)-\left(1-\frac{H}{2R}\right)\sigma_{rs}\left(s,x,-\frac{H}{2}\right),\\ \mathscr{P}_x &= \left(1+\frac{H}{2R}\right)\sigma_{rx}\left(s,x,\frac{H}{2}\right)-\left(1-\frac{H}{2R}\right)\sigma_{rx}\left(s,x,-\frac{H}{2}\right).\end{aligned} \tag{32}$$

Multiplication of $(4)_2$ and $(4)_3$ by $z(R+z)/R$ and integration through the thickness of the shell results in the following shell equilibrium equations

$$\frac{\partial M_s}{\partial s}+\frac{\partial M_{xs}}{\partial x}-Q_s+\mathscr{T}_s=0, \tag{33}$$

$$\frac{\partial M_x}{\partial x}+\frac{\partial M_{sx}}{\partial s}-Q_x+\mathscr{T}_x=0, \tag{34}$$

where $\mathscr{T}_s$ and $\mathscr{T}_x$ are the applied moment per unit midsurface area due to the circumferential and axial components, respectively, of the tractions on the top and bottom surfaces

$$\begin{aligned}\mathscr{T}_s &= \left(\frac{H}{2}+\frac{H^2}{4R}\right)\sigma_{rs}\left(s,x,\frac{H}{2}\right)+\left(\frac{H}{2}-\frac{H^2}{4R}\right)\sigma_{rs}\left(s,x,-\frac{H}{2}\right),\\ \mathscr{T}_x &= \left(\frac{H}{2}+\frac{H^2}{4R}\right)\sigma_{rx}\left(s,x,\frac{H}{2}\right)+\left(\frac{H}{2}-\frac{H^2}{4R}\right)\sigma_{rx}\left(s,x,-\frac{H}{2}\right).\end{aligned} \tag{35}$$

The displacement field for the classical and shear deformable shell theories are written in unified form using tracers as

$$\begin{aligned}u_s(s,x,z) &= u_s^0(s,x)+z\psi_s(s,x),\\ u_x(s,x,z) &= u_x^0(s,x)+z\psi_x(s,x),\\ u_r(s,x) &= u_r^0(s,x),\end{aligned} \tag{36}$$

where u_s^0, u_x^0 and u_r^0 are the midsurface displacements and ψ_s, ψ_x have the following definitions:

$$\begin{aligned}\psi_s(s,x) &= c_s\varphi_s(s,x)+(1-c_s)\left(\frac{u_s^0(s,x)}{R}-\frac{\partial u_r^0(s,x)}{\partial s}\right),\\ \psi_x(s,x) &= c_s\varphi_x(s,x)+(1-c_s)\left(-\frac{\partial u_r^0(s,x)}{\partial x}\right).\end{aligned} \tag{37}$$

The tracer $c_s=0$ for the classical deformation theory (CDT), wherein the transverse shear strains are zero. The first-order shear deformation theory (FSDT) is obtained by setting $c_s=1$. The quantities $-\varphi_s$ and φ_x in (37) are the rotations of the midsurface normals about the x and s-axis, respectively, for a shear deformable shell. In the classical deformation theory, due to the assumption of zero transverse shear deformation, the rotation of the normal is related to the slope of the midsurface after deformation. Therefore, the rotations of the midsurface normals in the classical deformation theory are $-u_s^0(s,x)/R+\partial u_r^0(s,x)/\partial s$ and $\partial u_r^0(s,x)/\partial x$ about the x and s-axis, respectively. Substitution of (36) into (8) yields the strains

$$\begin{aligned}\varepsilon_{ss} &= \left(1+\frac{z}{R}\right)^{-1}\left(\frac{\partial u_s^0}{\partial s}+z\frac{\partial \psi_s}{\partial s}+\frac{1}{R}u_r^0\right), \quad \varepsilon_{xx}=\left(\frac{\partial u_x^0}{\partial x}+z\frac{\partial \psi_x}{\partial x}\right),\\ \varepsilon_{sx} &= \frac{1}{2}\left[\frac{\partial u_s^0}{\partial x}+z\frac{\partial \psi_s}{\partial x}+\left(1+\frac{z}{R}\right)^{-1}\left(\frac{\partial u_x^0}{\partial s}+z\frac{\partial \psi_x}{\partial s}\right)\right], \quad \varepsilon_{xr}=\frac{1}{2}\left(\frac{\partial u_r^0}{\partial x}+\psi_x\right),\\ \varepsilon_{sr} &= \frac{1}{2}\left(1+\frac{z}{R}\right)^{-1}\left(\frac{\partial u_r^0}{\partial s}+\psi_s-\frac{u_s^0}{R}\right).\end{aligned} \tag{38}$$

The stresses are computed using the following plane-stress reduced constitutive relations (Reddy, 2003):

$$\begin{Bmatrix} \sigma_{ss} \\ \sigma_{xx} \\ \sigma_{sx} \end{Bmatrix} = \begin{bmatrix} \bar{Q}_{11} & \bar{Q}_{12} & \bar{Q}_{16} \\ \bar{Q}_{12} & \bar{Q}_{22} & \bar{Q}_{26} \\ \bar{Q}_{16} & \bar{Q}_{26} & \bar{Q}_{66} \end{bmatrix} \begin{Bmatrix} \varepsilon_{ss} - \alpha_{11} T \\ \varepsilon_{xx} - \alpha_{22} T \\ 2\varepsilon_{sx} - 2\alpha_{12} T \end{Bmatrix},$$
$$\begin{Bmatrix} \sigma_{xr} \\ \sigma_{sr} \end{Bmatrix} = \begin{bmatrix} \bar{Q}_{44} & \bar{Q}_{45} \\ \bar{Q}_{45} & \bar{Q}_{55} \end{bmatrix} \begin{Bmatrix} 2\varepsilon_{xr} \\ 2\varepsilon_{sr} \end{Bmatrix}, \tag{39}$$

where $\bar{Q}_{ij}$ are the reduced off-axis stiffness coefficients that can be computed from the three-dimensional elastic stiffnesses C_{ij} (Reddy, 2003). Following Reissner (1945), we multiply the integrals for the transverse shear force Q_x and Q_s in $(27)_3$ by a constant $\mathscr{K}$, known as the shear correction factor. In the present analysis, we set $\mathscr{K} = 5/6$, although this value was proposed by Reissner (1945) for a homogeneous plate or shell.

In the first-order shear deformation theory, the five shell equilibrium equations (28), (30), (31), (33) and (34) are necessary to obtain the five kinematic quantities $u_s^0(s,x), u_x^0(s,x), u_r^0(s,x)$, $\varphi_s(s,x)$ and $\varphi_x(s,x)$. In the classical deformation theory, the transverse shear force resultants are eliminated by inserting Q_x and Q_s from (33) and (34) into (28) and (30) and (31). The resulting equilibrium equations are

$$\begin{aligned} &\frac{\partial^2 M_x}{\partial x^2} + \frac{\partial^2 (M_{sx} + M_{xs})}{\partial s \partial x} + \frac{\partial^2 M_s}{\partial s^2} + \frac{\partial \mathscr{T}_s}{\partial s} + \frac{\partial \mathscr{T}_x}{\partial x} - \frac{N_s}{R} + \mathscr{P}_r = 0, \\ &\frac{\partial N_s}{\partial s} + \frac{\partial N_{xs}}{\partial x} + \frac{1}{R}\left(\frac{\partial M_s}{\partial s} + \frac{\partial M_{xs}}{\partial x} + \mathscr{T}_s\right) + \mathscr{P}_s = 0, \\ &\frac{\partial N_{sx}}{\partial s} + \frac{\partial N_x}{\partial x} + \mathscr{P}_x = 0. \end{aligned} \tag{40}$$

4.2. Donnell shell theory

The Donnell shallow shell theory (Donnell, 1935) is based on the stipulation that the thickness of the shell, H, is very small compared to its radius of curvature R, i.e., $H/R \ll 1$ and $|z/R| \ll 1$. The Donnell theory is obtained from the Flügge by neglecting z/R in the force and moment resultant integrals (25)–(27) and in the kinematic assumptions for u_s in the classical deformation theory obtained by the substitution of ψ_s from (37) into (36). Similarly, $H/2R$ in (29) and (32), and $H^2/4R$ in (35) are neglected. Furthermore, in the Donnell shell theory, the transverse shear force term Q_s/R is assumed to be negligible compared to the other terms in (30). Consequently, the term $(\partial M_s/\partial s + \partial M_{xs}/\partial x + \mathscr{T}_s)/R$ is neglected in the classical deformation equilibrium equation $(40)_2$.

4.3. Cylindrical bending

The shell equations are specialized to the problem of a shell of infinite extent in the axial direction by setting $\partial(\cdot)/\partial x = 0$. We seek a semi-inverse solution to the midsurface displacements and rotations by assuming that

$$\begin{aligned} &u_r^0 = U_r \sin ps, \quad u_s^0 = U_s \cos ps, \quad u_x^0 = U_x \cos ps, \\ &\varphi_s = \Phi_s \cos ps, \quad \varphi_x = \Phi_x \cos ps, \end{aligned} \tag{41}$$

where U_s, U_x, U_r, Φ_s and Φ_x are constants. The strains and stresses corresponding to the assumed midsurface displacements and rotations (41) are obtained using (38) and (39). The force and moment resultants

which are obtained using (25)–(27) are substituted into equilibrium equations (28)–(34) to yield 5 linear algebraic equations for the 5 constants U_s, U_x, U_r, Φ_s, Φ_x for the first-order shear deformation theory. When the classical deformation theory is used, the force and moment resultants are substituted into (40) to obtain 3 linear algebraic equations for the 3 constants U_s, U_x and U_r.

5. Estimation of effective moduli of two-phase composites

There are several homogenization methods for estimating the effective properties of isotropic two-phase functionally graded materials, including the self-consistent scheme by Hill (1965). The self-consistent method draws its estimates through the solution of an elastic problem in which an ellipsoidal inclusion is embedded in a matrix possessing the effective material properties of the composite. The self-consistent scheme has been shown to perform well for intermediate volume fractions of realistic microstructures (Reiter et al., 1997). The self-consistent formulas for the effective thermal conductivity, κ, thermal expansion coefficient, α, Young's modulus, E, Poisson's ratio, ν, and density, ρ, are the same as those used earlier by Vel and Batra (2002). The effective properties of functionally graded fiber-reinforced composite materials are determined using the composite cylinders assemblage model, which is based on the simplifying assumption that the composite material is filled with an assemblage of cylindrical fibers embedded in a concentric cylindrical matrix of different diameters such that the cylinders completely fill the volume of the composite (Hashin, 1979). The shear modulus G_{23} is estimated using the upper bound obtained by Hashin (1979).

6. Results and discussion

We present results for the analytical three-dimensional solution for the thermoelastic response of representative functionally graded shells. As stated in the problem formulation, the shells are of infinite extent in the axial direction and simply supported at the edges. We compare the predictions of Flügge's shell theory and Donnell's shell theory with the analytical solution for either continuous isotropic or orthotropic functional grading. We consider continuous volume fraction distributions of particulate or fiber-reinforcement, and, in the case the fiber-reinforced orthotropic shells, we also investigate continuous grading of fiber orientation through the shell's thickness. Results are provided at key locations for different geometric configurations and volume fraction variations. Tabulated analytical results are also presented at selected points for representative functionally graded cylindrical shells.

The isotropic functionally graded shells considered in the examples are assumed to be composed of aluminum and silicon carbide. We also study orthotropic functionally graded shells made of continuous tungsten reinforcement fibers in a copper matrix. These material combinations have found widespread use in high performance applications (Miracle, 2001). The relevant material properties for the constituent materials are listed in Table 1. We assume the material properties are independent of the temperature. Results are generated through the application of either a mechanical or temperature load on the top surface of the representative shell having non-zero components of the form,

Table 1
Material properties of aluminum, silicon carbide, copper and tungsten

	Al	SiC	Cu	W
E (GPa)	70.0	427.0	115.0	400.0
ν	0.30	0.17	0.31	0.28
α (10^{-6}/K)	23.4	4.30	17.0	4.40
κ (W/m K)	233.0	65.0	391.0	163.0

Table 2
Convergence study for a Al/SiC isotropic FGM shell employing the self-consistent scheme

Number of series terms	$\hat{u}_r(S/2,0)$	$\hat{\sigma}_{ss}(S/2,-H/2)$	$\hat{\sigma}_{rr}(S/2,0)$	$\hat{\sigma}_{sr}(0,0)$	$\hat{T}(S/2,0)$	$\hat{q}_r(S/2,0)$
2	4.547814	85.90864	−2.079126	0.8210083	0.4418832	0.6095894
4	4.569285	86.33582	−2.103852	0.8335770	0.4417561	0.6095698
6	4.569843	86.33649	−2.104001	0.8337424	0.4417559	0.6095701
8	4.569845	86.33650	−2.104001	0.8337428	0.4417559	0.6095701
10	4.569845	86.33650	−2.104001	0.8337428	0.4417559	0.6095701
12	4.569845	86.33650	−2.104001	0.8337428	0.4417559	0.6095701

The shell is partitioned into 20 layers in order to improve convergence. Fixed shell parameters are $R = 1$ m, $\Theta = 3\pi/4, S/H = 3, V_{\mathrm{SiC}}^{+} = 0.8, V_{\mathrm{SiC}}^{-} = 0.2, n = 2$.

$$\sigma_{rr}(s,x,H/2) = P^{+}\sin \pi s/S, \quad \text{or} \quad T(s,x,H/2) = T^{+}\sin \pi s/S, \tag{42}$$

and all other traction components on the top and bottom surfaces of the shell are set to zero. The inner surface $z = -H/2$ is held at the ambient reference temperature. Since the analysis is based on linear

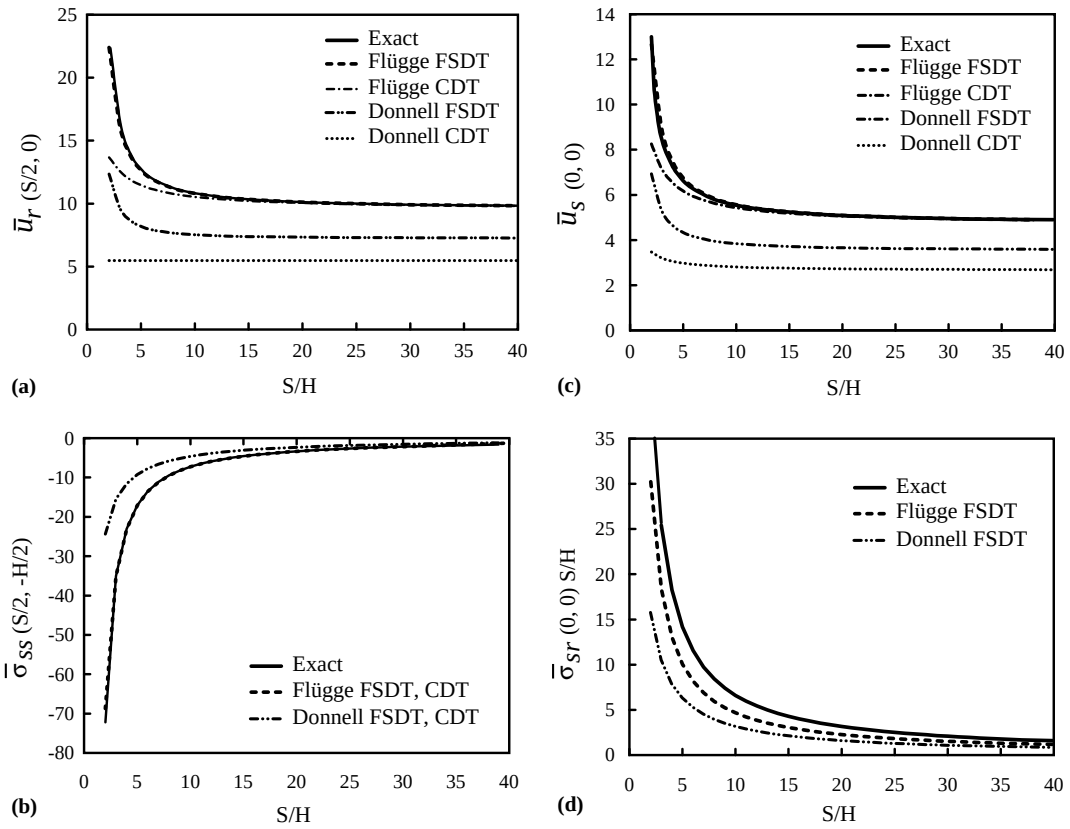

Fig. 3. Mechanical response for isotropic FGM Al/SiC cylindrical shells of varying length to thickness ratio. Shell parameters are $R = 1$ m, $\Theta = \pi/2, V_{\mathrm{SiC}}^{+} = 0.8, V_{\mathrm{SiC}}^{-} = 0.2, n = 2$.

thermoelasticity, results for combined thermomechanical loading may be determined through the superposition of results of separate analyses of thermal and mechanical loading cases.

The analytical solution presented here is applicable for arbitrary variation of material composition through the thickness of the shell. However, for the representative shells considered in the examples, we assume the following specific power-law variation of the reinforcement volume fraction

$$V = V^- + (V^+ - V^-)\left(\frac{1}{2} + \frac{z}{H}\right)^n, \tag{43}$$

where V^- and V^+, which have values that range from 0 to 1, denote the volume fractions on the inner and outer surfaces of the shell, respectively. The exponent n controls the volume fraction profile through the shell's thickness. Vel and Batra (2002) have used a similar scheme to define the volume fraction distribution for a plate. For orthotropic shells, the fiber orientation ϕ with respect to the s-axis in the $s - x$ surface is also assumed to have a power-law variation,

$$\phi = \phi^- + (\phi^+ - \phi^-)\left(\frac{1}{2} + \frac{z}{H}\right)^m, \tag{44}$$

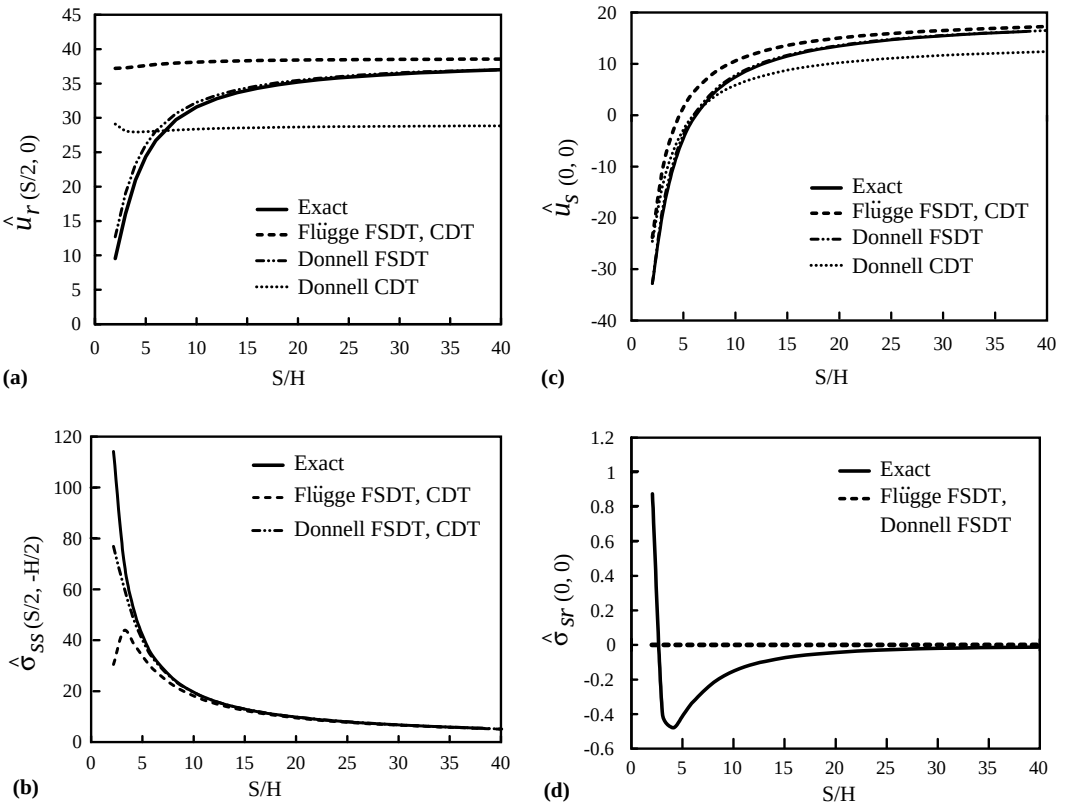

Fig. 4. Thermal response for isotropic FGM Al/SiC cylindrical shells of varying length to thickness ratio. Shell parameters are $R = 1$ m, $\Theta = \pi/2, V^+_{\mathrm{SiC}} = 0.8, V^-_{\mathrm{SiC}} = 0.2, n = 2$.

where ϕ^- and ϕ^+ denote the fiber orientations on the inner and outer surfaces, respectively, and may typically range from 0° to 360°. The power m denotes the manner in which the orientation of the tungsten fibers varies through the shell's thickness.

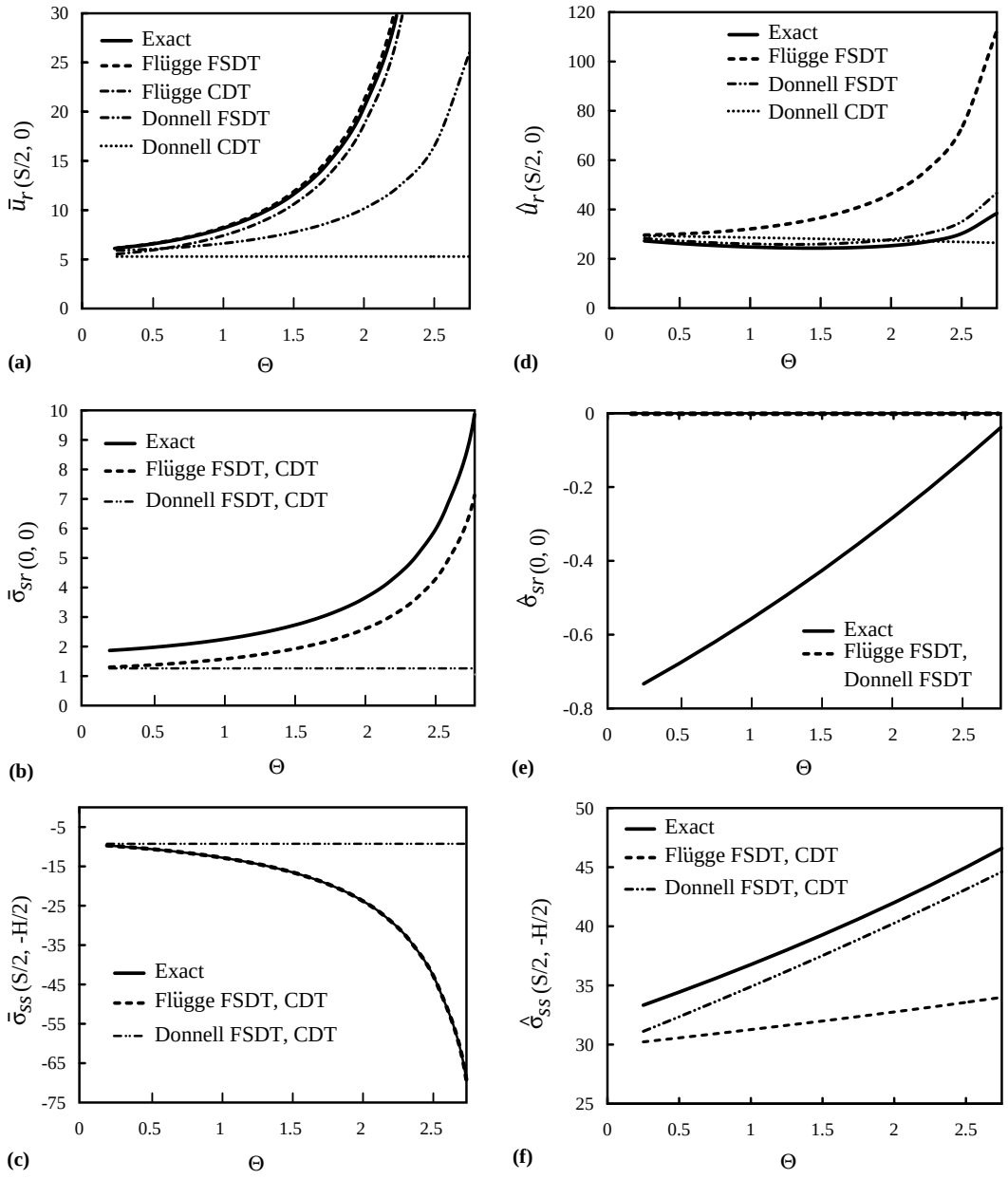

Fig. 5. Thermomechanical response for isotropic FGM Al/SiC cylindrical shells of varying angular extent. Shell parameters are $S/H = 5, R = 1$ m, $V^+_{SiC} = 0.8, V^-_{SiC} = 0.2$, $n = 2$.

The temperature, heat flux, displacements and stresses are presented in the following non-dimensional form for temperature loads

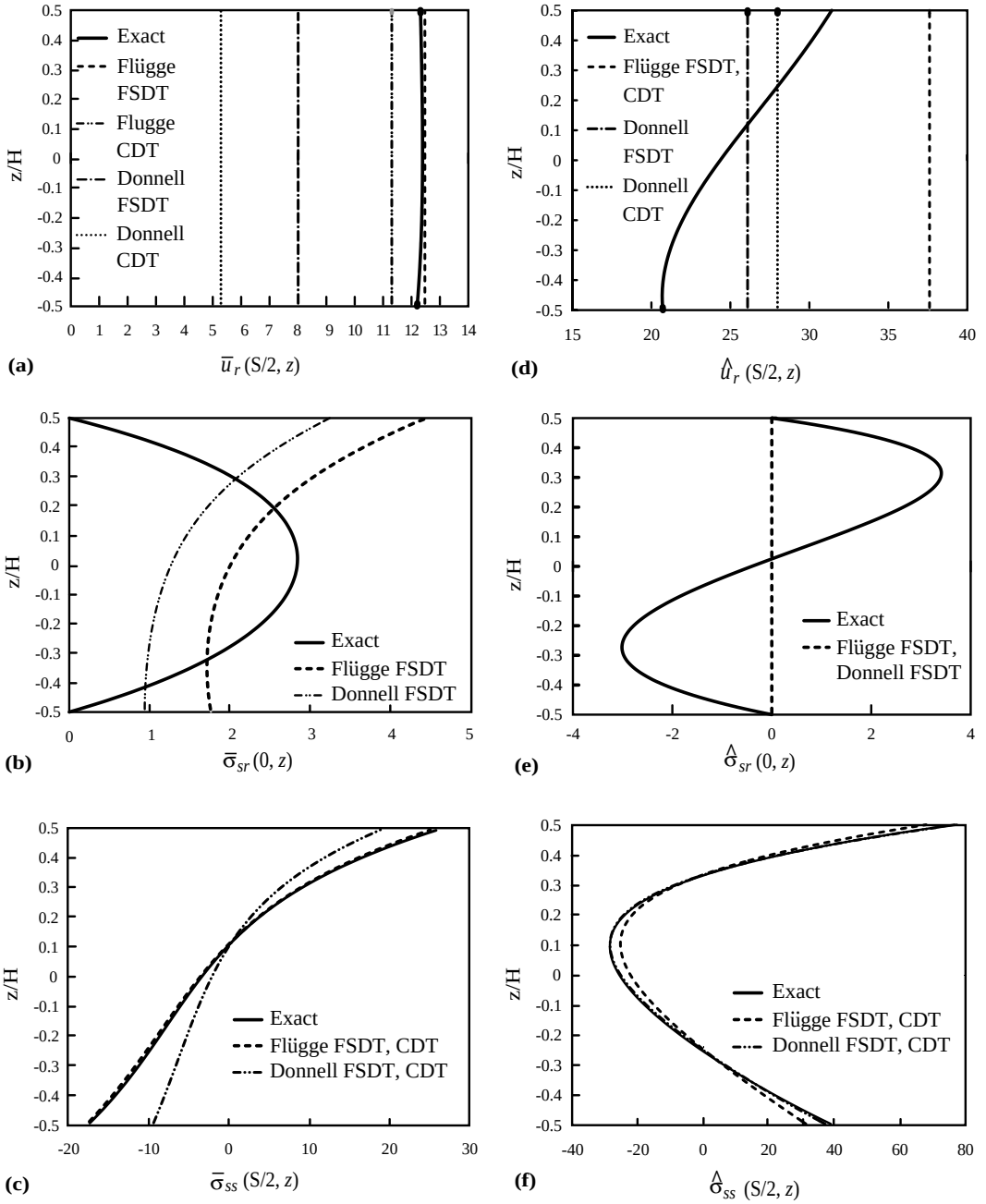

Fig. 6. Through-the-thickness plots for an isotropic FGM Al/SiC cylindrical shell under thermomechanical loading. Shell parameters are $S/H = 5, R = 1$ m, $\Theta = \pi/2$, $V^{+}_{\mathrm{SiC}} = 0.8$, $V^{-}_{\mathrm{SiC}} = 0.2$, $n = 2$.

$$\hat{T}(s,z) = \frac{1}{T^+}T(s,x,z), \quad \hat{\mathbf{q}}(s,z) = \frac{-H}{T^+\kappa_m}\mathbf{q}(s,x,z),$$
$$\hat{\mathbf{u}}(s,z) = \frac{1000H}{\alpha_m T^+ S^2}\mathbf{u}(s,x,z), \quad \hat{\boldsymbol{\sigma}}(s,z) = \frac{1000H}{E_m\alpha_m T^+ S}\boldsymbol{\sigma}(s,x,z), \tag{45}$$

where $z \in [-H/2,\ H/2]$ is the global thickness coordinate.

When the shell is subjected to a mechanical load, the results are non-dimensionalized as

$$\bar{\mathbf{u}}(s,z) = \frac{100E_m H^3}{P^+ S^4}\mathbf{u}(s,x,z), \quad \bar{\boldsymbol{\sigma}}(s,z) = \frac{100H^3}{P^+ S^3}\boldsymbol{\sigma}(s,x,z). \tag{46}$$

6.1. Isotropic functionally graded shells

We consider the functionally graded shell as a single inhomogeneous isotropic layer and employ our analytical power series solution for the analysis of a variety of shell geometries. We choose the silicon carbide volume fractions on the inner and outer surfaces to be $V^- = 0.2$, $V^+ = 0.8$ and a quadratic volume fraction profile in the radial direction with $n = 2$. We use the self-consistent scheme to estimate the spatially varying effective material properties (Hill, 1965). As shown in Table 2, a convergence study was conducted for the thermomechanical response of a very thick and deep shell having the above mentioned volume fraction distributions, $S/H = 3$, $R = 1$ m and $\Theta = 3\pi/4$. The computed exact results for the temperature, the heat flux, the displacements and the stresses of a functionally graded shell as $R \to \infty$ are identical to those presented by Vel and Batra (2003b) for a flat plate. In order to improve convergence and increase computational efficiency, the shell is divided into a total of 20 layers by the introduction of fictitious interfaces. The numerical results are shown in Table 2 for $2, 4, 6, 8, 10$ and 12 series terms per layer in (17) and (23). It clearly demonstrates that the displacements, stresses, temperature and heat flux have converged to 7 significant digits

Table 3
Tabular results for the mechanical response of Al/SiC isotropic FGM shells of varying geometry and volume fraction distribution using the self-consistent scheme

	$\Theta = \frac{\pi}{4}, \frac{S}{H} = 20$			$\Theta = \frac{\pi}{2}, \frac{S}{H} = 10$			$\Theta = \frac{3\pi}{4}, \frac{S}{H} = 5$		
n	1	2	3	1	2	3	1	2	3
$\bar{u}_r(S/2,-H/2)$	5.5317	6.1935	6.4928	9.3887	10.534	11.054	34.234	38.750	40.827
$\bar{u}_r(S/2,0)$	5.5394	6.2028	6.5025	9.4279	10.581	11.103	34.493	39.054	41.138
$\bar{u}_r(S/2,H/2)$	5.5368	6.1999	6.4992	9.4127	10.563	11.083	34.345	38.881	40.939
$\bar{u}_s(0,-H/2)$	1.8635	2.0919	2.1873	5.9736	6.7120	7.0263	30.698	34.720	36.493
$\bar{u}_s(0,0)$	1.4597	1.6403	1.7138	4.9053	5.5186	5.7740	26.547	30.088	31.610
$\bar{u}_s(0,H/2)$	1.0553	1.1878	1.2397	3.8307	4.3170	4.5153	22.298	25.338	26.637
$\bar{\sigma}_{rr}(S/2,0)$	−0.026452	−0.025532	−0.025159	−0.29092	−0.28107	−0.27701	−3.4672	−3.3457	−3.2915
$\bar{\sigma}_{ss}(S/2,-H/2)$	−2.3108	−2.6133	−2.7119	−6.5434	−7.3910	−7.6682	−30.971	−34.887	−36.212
$\bar{\sigma}_{ss}(S/2,0)$	−0.62966	−0.56321	−0.48379	−1.6780	−1.5084	−1.2989	−6.6887	−6.0965	−5.2788
$\bar{\sigma}_{ss}(S/2,H/2)$	4.6932	5.1666	5.4938	11.828	13.030	13.858	40.911	45.177	48.049
$\bar{\sigma}_{xx}(S/2,-H/2)$	−0.64383	−0.72811	−0.75557	−1.8230	−2.0592	−2.1364	−8.6290	−9.7199	−10.089
$\bar{\sigma}_{xx}(S/2,0)$	−0.15483	−0.15220	−0.13689	−0.46465	−0.46263	−0.42388	−2.3966	−2.4410	−2.3052
$\bar{\sigma}_{xx}(S/2,H/2)$	0.90685	0.99809	1.0611	2.2987	2.5304	2.6900	8.0384	8.8605	9.4138
$\bar{\sigma}_{sr}(0,0)$	0.12803	0.12542	0.12325	0.68058	0.66159	0.65447	5.3029	5.1459	5.0803
$\bar{\sigma}_{sr}(0,H/4)$	0.11434	0.11384	0.11236	0.57444	0.57214	0.56459	3.8955	3.8827	3.8274

Fixed shell parameters are $R = 1$ m, $V^+_{\mathrm{SiC}} = 0.8, V^-_{\mathrm{SiC}} = 0.2$.

Table 4
Tabular results for the thermal response of Al/SiC isotropic FGM shells of varying geometry and volume fraction distribution using the self-consistent scheme

	$\Theta = \frac{\pi}{4}, \frac{S}{H} = 20$			$\Theta = \frac{\pi}{2}, \frac{S}{H} = 10$			$\Theta = \frac{3\pi}{4}, \frac{S}{H} = 5$		
n	1	2	3	1	2	3	1	2	3
$\hat{u}_r(S/2, -H/2)$	29.371	29.362	31.971	32.023	30.703	33.109	32.355	24.081	24.259
$\hat{u}_r(S/2, 0)$	29.536	29.575	32.209	32.713	31.589	34.096	35.375	27.986	28.637
$\hat{u}_r(S/2, H/2)$	29.895	30.011	32.715	34.165	33.354	36.146	41.312	35.197	37.001
$\hat{u}_s(0, -H/2)$	6.2454	5.5538	5.9073	13.793	11.753	12.358	19.805	10.908	9.8940
$\hat{u}_s(0, 0)$	4.0109	3.3024	3.4518	9.4591	7.4320	7.6609	12.047	3.5032	1.9314
$\hat{u}_s(0, H/2)$	1.7574	1.0295	0.97269	4.9591	2.9367	2.7721	3.0247	−5.3432	−7.6098
$\hat{\sigma}_{rr}(S/2, 0)$	-1.7832×10^{-3}	2.6731×10^{-3}	8.0553×10^{-3}	−0.018151	0.015962	0.058741	−0.27393	−0.17460	0.029254
$\hat{\sigma}_{ss}(S/2, -H/2)$	5.2757	8.5910	10.026	11.347	18.407	21.451	27.506	44.103	51.183
$\hat{\sigma}_{ss}(S/2, 0)$	−3.3108	−5.6959	−6.7723	−6.9527	−11.917	−14.158	−15.558	−26.343	−31.192
$\hat{\sigma}_{ss}(S/2, H/2)$	7.8633	18.656	29.108	16.133	37.929	58.969	34.393	78.901	121.49
$\hat{\sigma}_{xx}(S/2, -H/2)$	1.4698	2.3935	2.7935	3.1615	5.1284	5.9766	7.6635	12.287	14.260
$\hat{\sigma}_{xx}(S/2, 0)$	−24.698	−24.463	−24.864	−50.724	−50.277	−51.076	−107.39	−106.55	−108.06
$\hat{\sigma}_{xx}(S/2, H/2)$	−57.847	−55.867	−53.853	−115.81	−111.61	−107.56	−231.22	−222.64	−214.43
$\hat{\sigma}_{sr}(0, 0)$	−0.011956	−0.045917	−0.076992	−0.027748	−0.14933	−0.26630	0.14185	−0.16890	−0.54432
$\hat{\sigma}_{sr}(0, H/4)$	0.099692	0.18525	0.23179	0.41416	0.76719	0.96071	1.7996	3.2940	4.1233
$\hat{T}(S/2, 0)$	0.40521	0.40604	0.41762	0.41576	0.41678	0.42844	0.43906	0.44018	0.45161
$\hat{T}(S/2, H/4)$	0.67212	0.65835	0.65951	0.68056	0.66714	0.66835	0.69775	0.68491	0.68595
$\hat{q}_r(S/2, -H/2)$	0.55604	0.63055	0.67274	0.58772	0.66608	0.70989	0.67568	0.76339	0.81087
$\hat{q}_r(S/2, 0)$	0.54665	0.62001	0.66155	0.54802	0.62155	0.66270	0.54625	0.61936	0.65907
$\hat{q}_r(S/2, H/2)$	0.53979	0.61220	0.65334	0.52173	0.59162	0.63130	0.48732	0.55239	0.58967
$\hat{q}_s(0, H/4)$	0.048140	0.055126	0.061769	0.094726	0.10856	0.12164	0.18058	0.20724	0.23215

Fixed shell parameters are $R = 1$ m, $V^{+}_{\mathrm{SiC}} = 0.8, V^{-}_{\mathrm{SiC}} = 0.2$.

Table 5
Convergence study for a W/Cu orthotropic fiber FGM shell, which is partitioned into 20 layers in order to improve convergence

Number of series terms	$\hat{u}_r(S/2,0)$	$\hat{\sigma}_{ss}(S/2,-H/2)$	$\hat{\sigma}_{rr}(S/2,0)$	$\hat{\sigma}_{sr}(0,0)$	$\hat{T}(S/2,0)$	$\hat{q}_r(S/2,H/4)$
2	50.07721	26.65748	−0.6199901	−0.1437777	0.5299225	0.5047100
4	50.07659	26.66727	−0.6286236	−0.1370722	0.5298581	0.5048625
6	50.07689	26.66743	−0.6286748	−0.1369956	0.5298579	0.5048627
8	50.07689	26.66743	−0.6286748	−0.1369956	0.5298579	0.5048627
10	50.07689	26.66743	−0.6286748	−0.1369956	0.5298579	0.5048627
12	50.07689	26.66743	−0.6286748	−0.1369956	0.5298579	0.5048627

Fixed shell parameters are $R = 1$ m, $\Theta = 3\pi/4$, $S/H = 3$, $V_W = 0.75$, $m = 1$.

with 10 series terms per layer. All numerical results and plots shown henceforth are obtained using 20 fictitious layers and 10 series terms per layer.

Fig. 3 depicts the stresses and displacements at specific points as a function of the shell's circumferential width-to-thickness ratio (S/H), due to the sinusoidally distributed pressure load $(42)_1$. The angular span and midsurface radius are chosen to be $\Theta = \pi/2$ and $R = 1$, respectively. The midsurface radial displacement $\bar{u}_r(S/2,0)$ is accurately predicted by the Flügge shell theory with FSDT. This is observed over the entire range of shell length to thickness ratios. As the shell becomes increasingly thick, Flügge CDT tends to underestimate the displacements for length to thickness ratios less than 10. The radial displacement of the Donnell shell theory is offset by a constant value and presents significant error throughout the entire range of width-to-thickness ratios investigated, although the Donnell FSDT performs better than the Donnell CDT. The midsurface edge displacement in the lateral direction $\bar{u}_s(0,0)$ follows identical trends. Flügge's shell theory accurately captures the circumferential normal stress $\bar{\sigma}_{ss}(S/2,-H/2)$ over the entire range of length to thickness ratios for both CDT as well as FSDT. In general, Flügge and Donnell FSDT underestimate the transverse shear stresses $\bar{\sigma}_{sr}(0,0)$ over the entire range of shell width-to-thickness ratios as demonstrated in Fig. 3(d). The thermal deformation and stresses are shown in Fig. 4 as a function of the shell's circumferential width-to-thickness ratio when it is subjected to the temperature load $(42)_2$. Donnell's shell theory is found to predict the displacements $\hat{u}_r$ and $\hat{u}_s$ and circumferential normal stress $\hat{\sigma}_{ss}$ better than Flügge's shell theory. The transverse shear stress at the shell's midsurface, $\hat{\sigma}_{sr}(0,0)$, which is predicted to be zero by the FSDT, exhibits serious discrepancy when compared to the analytical solution. However, it is noted that the magnitude of the transverse shear stress $\hat{\sigma}_{sr}$ is much smaller than the circumferential normal stress $\hat{\sigma}_{ss}$.

The response of isotropic graded shells as a function of the angular extent is presented in Fig. 5, where the shell's midsurface radius, R, the volume fraction power-law exponent, n, and width-to-thickness ratio, S/H, have fixed values of 1 m, 2 and 5, respectively. The neglect of shear deformation in the Flügge CDT theory leads to slightly less accurate predictions of the midsurface displacements as detailed in Fig. 5(a). The Flügge FSDT theory demonstrates excellent correlation for the circumferential normal stress, $\bar{\sigma}_{ss}$, over the entire range of shell opening angles as shown in Fig. 5(c). The Donnell shell theory does not give accurate results for the radial displacement or circumferential normal stress for shells with angular extents greater than 0.5 radians. Results for the temperature loads in Fig. 5(d)–(f), indicate that Donnell's shell theory does better than Flügge's theory in predicting the thermal displacements and stresses.

The through-the-thickness variation of displacements and stresses are depicted in Fig. 6 for a moderately thick shell with angular extent of $\Theta = \pi/2$, width-to-thickness ratio $S/H = 5$, midsurface radius $R = 1$ m and volume fraction profile defined by $n = 2$. It demonstrates that when the shell is subjected to a radial pressure load, the assumption of constant radial displacement through the thickness of the shell is valid. However, when the shell is subjected to a thermal load, the radial displacement is not constant due to

thermal expansion in the radial direction. The through-the-thickness profiles of the transverse shear stress $\sigma_{sr}(0, z/H)$ predicted by the Flügge and Donnell FSDT theories are inaccurate.

Tables 3 and 4 present tabular data for the exact solution for the thermomechanical response of an isotropic cylindrical shell where the material properties have been obtained through use of the self-consistent

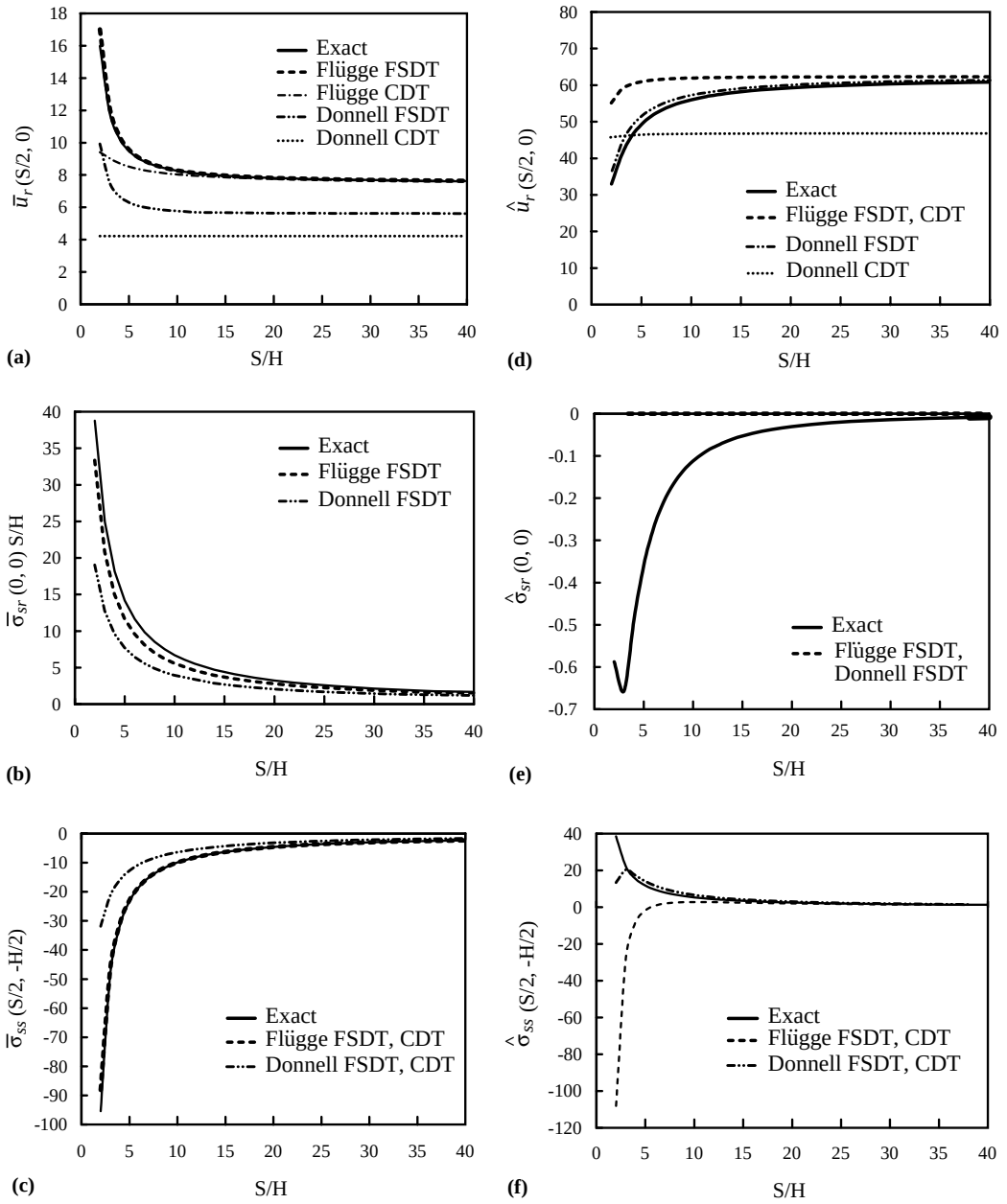

Fig. 7. Thermomechanical response for orthotropic FGM W/Cu cylindrical shells of varying length to thickness ratio. Shell parameters are $R = 1$ m, $\Theta = \pi/2, V_W^+ = 0.75, V_W^- = 0.75, \phi^- = 0°, \phi^+ = 180°, m = 1$.

scheme (Hill, 1965). Non-dimensionalized stress components, displacements, temperatures and heat flux are provided for mechanical and thermal cases for some common geometries.

6.2. Fiber-reinforced orthotropic functionally graded shells

The shell theories are compared to the analytical solution for orthotropic shells consisting of tungsten fibers in a copper matrix (W/Cu). The orientation of the tungsten fibers is chosen to be a smooth function

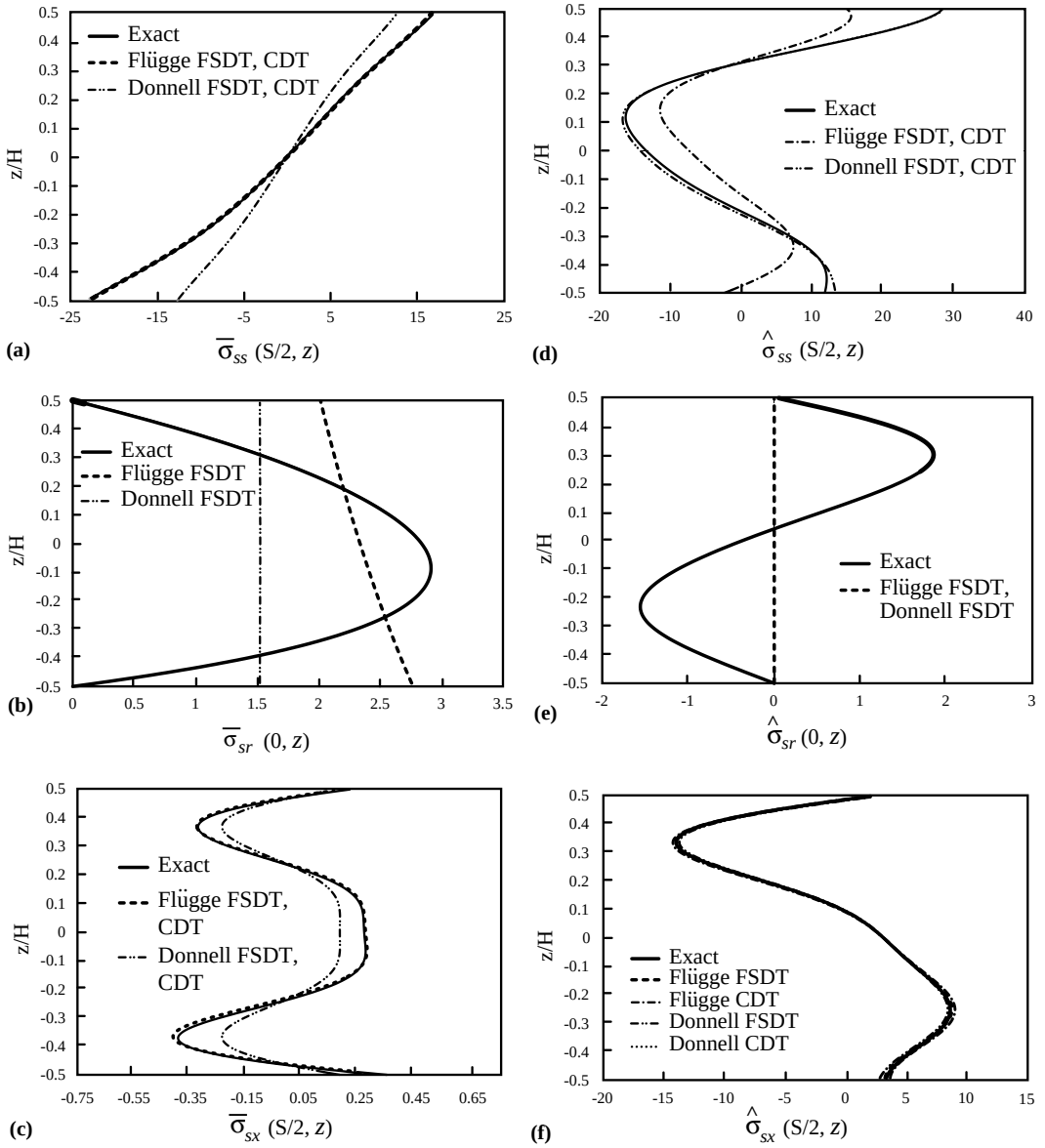

Fig. 8. Through-the-thickness plots for an orthotropic FGM W/Cu cylindrical shells under thermomechanical loading. Shell parameters are $S/H = 5$, $R = 1$ m, $\Theta = \pi/2, V_{\mathrm{W}}^{+} = 0.75, V_{\mathrm{W}}^{-} = 0.75, \phi^{-} = 0^{\circ}, \phi^{+} = 180^{\circ}$, $m = 1$.

of the shell's radial coordinate. The composite cylindrical assemblage model developed by Hashin (1979) is used to determine the spatially varying thermomechanical material properties, relative to the fiber's axial direction, as a function of the fiber volume fraction. Off-axis material properties in the global coordinate system are determined through appropriate tensor transformation of the principle material properties relative to the shell's circumferential direction, defined by the fiber orientation angle, ϕ. The results of a convergence study are shown in Table 5 for the thermomechanical response of a thick orthotropic shell with the fiber orientation varying linearly ($m = 1$) from $\phi^- = 0°$ on the inner surface to $\phi^+ = 180°$ on the outer surface. The fiber volume fraction is held constant at $V_W = 0.75$ throughout, and the geometric parameters are chosen to be $S/H = 3$, $R = 1$ m and $\Theta = 3\pi/4$. A convergence study is performed by dividing the shell into 20 fictitious layers through the thickness. As evinced by Table 5, the temperature, heat flux, displacements, stresses have converged to 7 significant digits with 10 series terms per layer.

Fig. 7 presents the results for mechanical and thermal loading of moderately deep W/Cu orthotropic shells having $R = 1$ m, $\Theta = \pi/2$ and material properties that are symmetric about the midsurface, as a function of the circumferential length-to-thickness ratios. The fiber orientation is assumed to vary linearly ($m = 1$) in the radial direction from $\phi^- = 0°$ and $\phi^+ = 180°$ and the fiber volume fraction is held constant at $V_W = 0.75$ throughout. As observed previously for isotropic shells, Flügge shell theory gives good results for mechanically applied surface loads, with the addition of shear deformation theory leading to the most accurate predictions of the midsurface radial displacements. However, the Donnell shell theory performs better for the thermal load. Through-the-thickness plots of the stresses for mechanical and thermal loads

Table 6
Tabular results for the mechanical response of W/Cu orthotropic FGM shells of varying geometry, volume fraction, and fiber orientation distributions

	$\Theta = \frac{\pi}{4}, \frac{S}{H} = 20$		$\Theta = \frac{\pi}{2}, \frac{S}{H} = 10$		$\Theta = \frac{3\pi}{4}, \frac{S}{H} = 5$	
n	0	1	0	1	0	1
m	1	1	1	3	3	1
$\bar{u}_r(S/2, -H/2)$	5.1102	8.2409	8.5535	13.659	29.673	50.624
$\bar{u}_r(S/2, 0)$	5.1155	8.2536	8.5795	13.723	29.818	51.061
$\bar{u}_r(S/2, H/2)$	5.1094	8.2465	8.5465	13.684	29.557	50.721
$\bar{u}_s(0, -H/2)$	1.6397	2.7370	5.2328	8.5879	25.882	45.013
$\bar{u}_s(0, 0)$	1.2652	2.1349	4.2447	7.0294	22.125	38.827
$\bar{u}_s(0, H/2)$	0.89078	1.5322	3.2559	5.4641	18.355	32.526
$\bar{u}_x(0, -H/2)$	-5.7619×10^{-3}	−0.011201	−0.015729	0.025406	0.056848	−0.12638
$\bar{u}_x(0, 0)$	-5.7218×10^{-3}	−0.011152	−0.015298	0.025788	0.061118	−0.11853
$\bar{u}_x(0, H/2)$	-5.6931×10^{-3}	−0.011087	−0.015010	0.026303	0.064792	−0.10977
$\bar{\sigma}_{rr}(S/2, 0)$	−0.025679	−0.026583	−0.28130	−0.29689	−3.3041	−3.4556
$\bar{\sigma}_{ss}(S/2, -H/2)$	−3.5664	−2.3993	−10.016	−6.6305	−45.812	−32.033
$\bar{\sigma}_{ss}(S/2, 0)$	0.10860	−0.40409	0.28080	−1.2087	0.94387	−4.3439
$\bar{\sigma}_{ss}(S/2, H/2)$	3.1129	4.2613	7.7718	10.512	25.604	36.899
$\bar{\sigma}_{xx}(S/2, -H/2)$	−0.86737	−0.74378	−2.4360	−2.0554	−11.141	−9.9302
$\bar{\sigma}_{xx}(S/2, 0)$	0.028582	−0.14099	0.015886	−0.39005	−0.72048	−2.3890
$\bar{\sigma}_{xx}(S/2, H/2)$	0.89512	1.2240	2.2545	3.0396	7.5624	10.797
$\bar{\sigma}_{sr}(0, 0)$	0.12915	0.12964	0.67922	0.69673	5.1953	5.3154
$\bar{\sigma}_{sr}(0, H/4)$	0.092671	0.10832	0.46078	0.54178	3.0120	3.6595
$\bar{\sigma}_{xr}(0, 0)$	2.3563×10^{-3}	2.8377×10^{-3}	0.012216	9.9401×10^{-3}	0.073341	0.10679
$\bar{\sigma}_{xr}(0, H/4)$	8.972×10^{-4}	1.4101×10^{-3}	4.4133×10^{-3}	6.0765×10^{-3}	0.030613	0.044030
$\bar{\sigma}_{sx}(S/2, -H/2)$	0.017297	0.013701	0.050240	−0.033061	−0.21888	0.19825
$\bar{\sigma}_{sx}(S/2, 0)$	0.023667	4.219×10^{-4}	0.065599	−0.089183	−0.12560	0.066576
$\bar{\sigma}_{sx}(S/2, H/2)$	0.016432	0.032004	0.040959	−0.71775	−0.15432	0.26147

Fixed shell parameters are $R = 1$ m, $V_W^+ = 0.75, V_W^- = 0, \phi^- = 0°, \phi^+ = 90°$.

Table 7
Tabular results for the thermal response of W/Cu orthotropic FGM shells of varying geometry, volume fraction, and fiber orientation distributions

	$\Theta = \frac{\pi}{4}, \frac{S}{H} = 20$		$\Theta = \frac{\pi}{2}, \frac{S}{H} = 10$		$\Theta = \frac{3\pi}{4}, \frac{S}{H} = 5$	
n	0	1	0	1	0	1
m	1	1	1	3	3	1
$\hat{u}_r(S/2, -H/2)$	58.433	57.116	67.783	61.800	84.928	74.169
$\hat{u}_r(S/2, 0)$	58.609	57.382	68.510	62.954	88.095	78.960
$\hat{u}_r(S/2, H/2)$	59.121	57.989	70.572	65.468	96.662	88.979
$\hat{u}_s(0, -H/2)$	14.889	13.432	34.443	29.787	64.964	52.037
$\hat{u}_s(0, 0)$	10.502	9.1164	25.787	21.724	49.795	36.815
$\hat{u}_s(0, H/2)$	6.0867	4.7672	16.906	13.357	32.629	19.380
$\hat{u}_x(0, -H/2)$	0.42087	0.61996	0.85335	1.6366	1.8170	2.6206
$\hat{u}_x(0, 0)$	0.42152	0.62079	0.85914	1.6546	1.9279	2.7047
$\hat{u}_x(0, H/2)$	0.42124	0.62012	0.85724	1.6630	1.9975	2.6762
$\hat{\sigma}_{rr}(S/2, 0)$	4.9287×10^{-3}	3.3892×10^{-3}	0.040736	−0.031550	0.084644	0.035258
$\hat{\sigma}_{ss}(S/2, -H/2)$	−2.7678	3.0014	−5.7832	4.1995	−16.011	16.323
$\hat{\sigma}_{ss}(S/2, 0)$	0.91879	−1.9402	1.9017	0.72776	12.303	−9.1328
$\hat{\sigma}_{ss}(S/2, H/2)$	−0.58778	7.7467	−1.2682	6.3149	−17.430	32.240
$\hat{\sigma}_{xx}(S/2, -H/2)$	−0.67316	0.93044	−1.4065	1.3018	−3.8941	5.0601
$\hat{\sigma}_{xx}(S/2, 0)$	−23.511	−21.168	−47.936	−48.855	−110.91	−91.515
$\hat{\sigma}_{xx}(S/2, H/2)$	−46.747	−44.360	−93.521	−91.349	−191.30	−177.08
$\hat{\sigma}_{sr}(0, 0)$	−0.014499	−0.026304	−0.064110	0.061276	0.049721	−0.19386
$\hat{\sigma}_{sr}(0, H/4)$	−0.023157	0.069293	−0.095122	−0.043928	−1.4419	1.2399
$\hat{\sigma}_{xr}(0, 0)$	0.011145	1.5202×10^{-3}	0.053947	0.31891	1.5882	0.15790
$\hat{\sigma}_{xr}(0, H/4)$	−0.019129	−0.031402	−0.069108	0.078596	0.58639	−0.38028
$\hat{\sigma}_{sx}(S/2, -H/2)$	−1.2634	−0.75827	−2.7255	−2.1297	−6.9963	−4.1110
$\hat{\sigma}_{sx}(S/2, 0)$	1.0600	1.1321	2.1648	−0.20032	2.7723×10^{-3}	4.7735
$\hat{\sigma}_{sx}(S/2, H/2)$	−1.2158	−1.7899	−2.3392	−4.5381	−4.7578	−6.3745
$\hat{T}(S/2, 0)$	0.50332	0.42462	0.51329	0.43490	0.53294	0.45763
$\hat{T}(S/2, H/4)$	0.75229	0.68972	0.75906	0.69766	0.77094	0.71387
$\hat{q}_r(S/2, -H/2)$	0.53650	0.73123	0.56246	0.77121	0.63150	0.88235
$\hat{q}_r(S/2, 0)$	0.52770	0.71898	0.52557	0.71966	0.51606	0.71530
$\hat{q}_r(S/2, H/2)$	0.52234	0.71031	0.50505	0.68692	0.47727	0.64244
$\hat{q}_s(0, 0)$	0.043125	0.050489	0.087959	0.10649	0.18797	0.21765
$\hat{q}_x(0, 0)$	1.3592×10^{-3}	1.6250×10^{-3}	2.7723×10^{-3}	1.2739×10^{-3}	2.2031×10^{-3}	7.0054×10^{-3}

Fixed shell parameters are $R = 1$ m, $V_{\mathrm{W}}^{+} = 0.75, V_{\mathrm{W}}^{-} = 0, \phi^{-} = 0^\circ, \phi^{+} = 90^\circ$.

are shown in Fig. 8. Tabulated thermoelastic results for the case of W/Cu fiber-reinforced graded shells are presented in Tables 6 and 7 for different geometries, fiber orientation profiles and volume fraction distributions.

6.3. Discretely laminated shells vs. continuous grading of fiber volume fraction and orientation

In this section, we characterize the response of orthotropic shells with continuous grading of fiber orientation and compare the results with conventional discretely laminated cylindrical shells. Specifically, we compare a graded shell with a linear variation of fiber orientation from $\phi^{-} = 0^\circ$ and $\phi^{+} = 90^\circ$ with 2-layer [0°/90°], 3-layer [0°/45°/90°] and 4-layer [0°/30°/60°/90°] discrete laminates. The through-the-thickness plots of the stresses for the four configurations are shown in Fig. 9 for a mechanical load. The circumferential non-dimensionalized normal stress for the graded fiber-reinforced shell is $\bar{\sigma}_{ss}(S/2, -H/2) = -23.454$, which is larger than the values of −23.169 and −22.366 obtained for the 2-layer and 3-layer shells, respectively. The 4-layer [0°/30°/60°/90°] shell exhibits the smallest circumferential

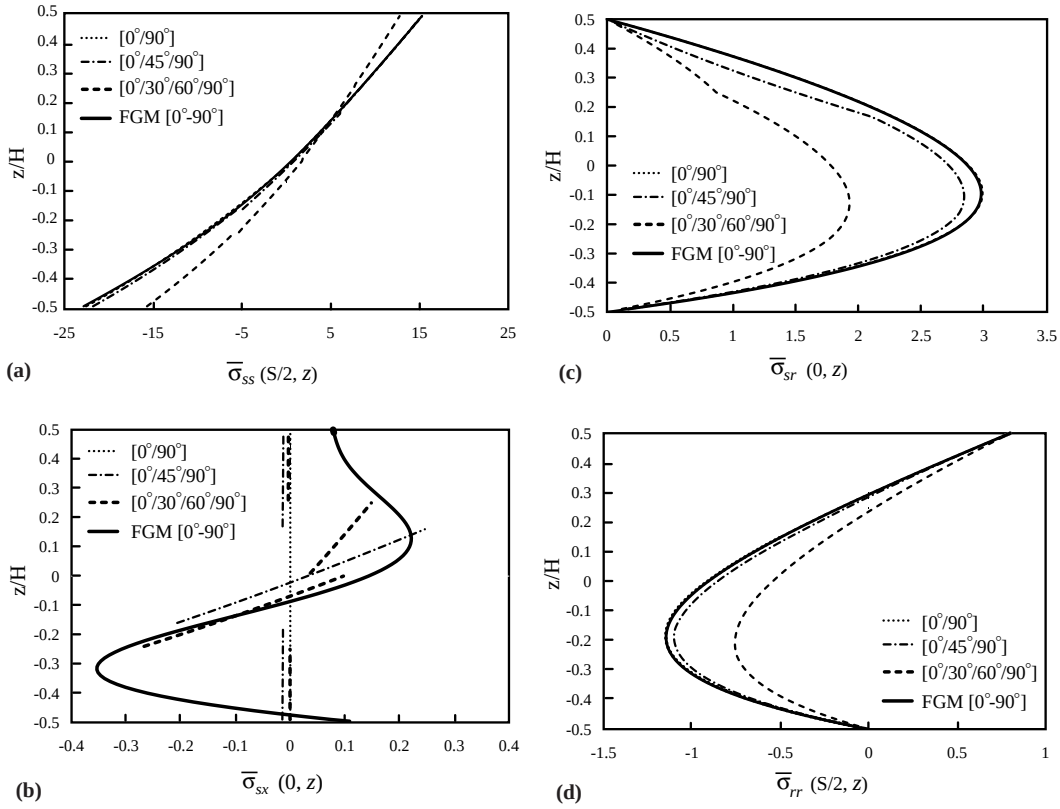

Fig. 9. Effect of linear graded fiber orientation on orthotropic W/Cu cylindrical shell stresses under mechanical loading. Shell parameters are $S/H = 5$, $R = 1$ m, $\Theta = \pi/2$, $V_{\mathrm{W}}^{+} = 0.75$, $V_{\mathrm{W}}^{-} = 0.75$.

normal stress $\bar{\sigma}_{ss}(S/2, -H/2) = -16.149$. The shear stress $\bar{\sigma}_{sx}$ has a smooth variation through the thickness of the graded fiber-reinforced shell as depicted in Fig. 9(b). The transverse shear stress $\bar{\sigma}_{sr}$ and transverse normal stress $\bar{\sigma}_{rr}$ are shown in Fig. 9(c) and (d).

Fig. 10, which contains the through-the-thickness plots of the stresses for a temperature load $(42)_2$, clearly illustrates the benefits of functionally graded fiber-reinforced shells. For the graded shell, the maximum circumferential stress $\hat{\sigma}_{ss} = -11.827$, which is much smaller than the maximum circumferential stresses of $\hat{\sigma}_{ss} = 25.048$, 232.07 and -1252.1, for the 2-layer, 3-layer and 4-layer shells, respectively. Thus, the functionally graded shell exhibits a 52.7% reduction in the circumferential normal stress magnitude as compared to the [0°/90°] discrete laminated shell. The maximum values of the transverse shear and transverse normal stresses are $[\hat{\sigma}_{sr}, \hat{\sigma}_{rr}] = [0.6436, -0.2871], [-1.3325, 0.77951], [-96.111, 15.412]$ and $[187.65, -68.871]$ for the FGM, 2-layer, 3-layer and 4-layer shells, respectively. The maximum shear stress for the graded shell $\hat{\sigma}_{sx} = -5.8450$, is larger than the value of $\hat{\sigma}_{sx} = 0$ for a [0°/90°] shell, but smaller than the maximum shear stresses of $\hat{\sigma}_{sx} = 10.234$ and -22.789 for the [0°/45°/90°] and [0°/30°/60°/90°] shells, respectively.

The effect of graded fiber volume fraction is considered next. Fig. 11 contains through-the-thickness plots of thermally induced stresses for shells having all of its fibers oriented at $\phi = 0°$, and geometry defined by $S/H = 5$, $R = 1$ m and $\Theta = \pi/2$. The functionally graded shell has a linear variation starting at $V_W = 0$ on the inner surface of the shell to $V_W = 0.75$ on the outer surface. The results are compared with discretely laminated 2-layer, 3-layer and 4-layer shells containing [0/0.75], [0/0.375/0.75] and [0/0.25/0.50/0.75]

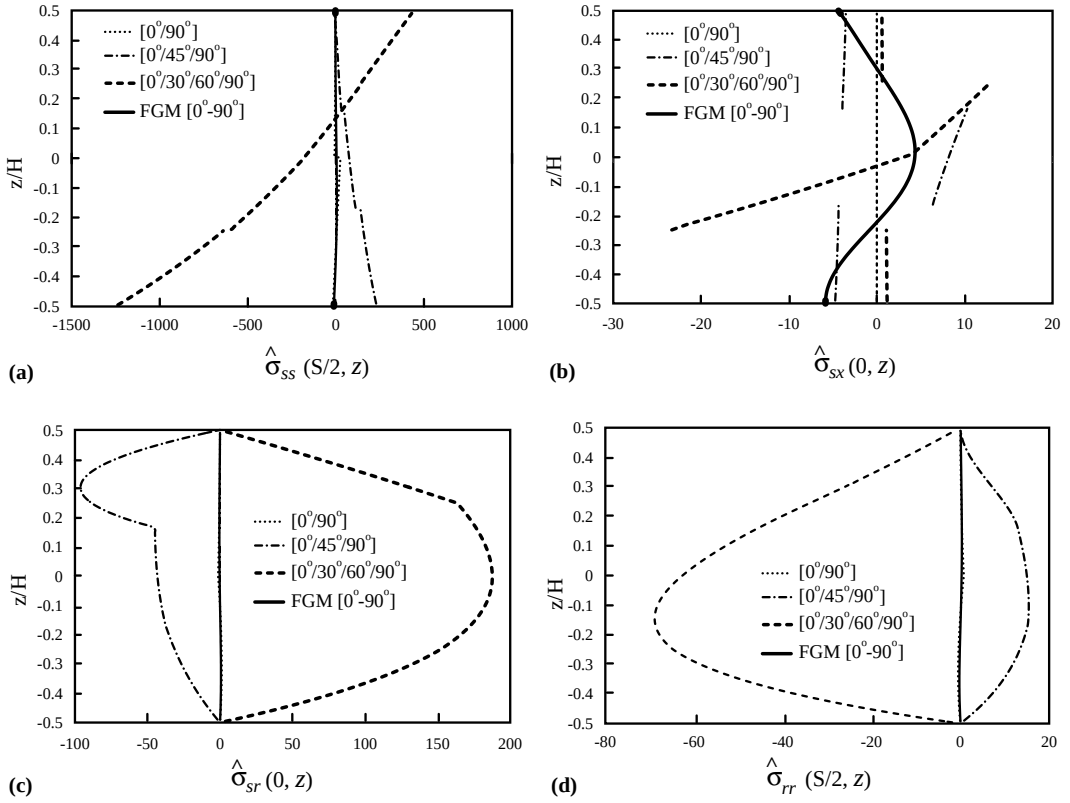

Fig. 10. Effect of linear graded fiber orientation on orthotropic W/Cu cylindrical shell stresses under thermal loading. Shell parameters are $S/H = 5$, $R = 1$ m, $\Theta = \pi/2$, $V_{\mathrm{W}}^{+} = 0.75$, $V_{\mathrm{W}}^{-} = 0.75$.

volume fractions, respectively. The peak non-dimensionalized circumferential stress magnitude for the graded shell is 21.844, which is smaller than the values of 56.002, 37.236 and 28.702 for the 2-layer, 3-layer and 4-layer shells, respectively. Fig. 11 also demonstrates how the axial stress $\bar{\sigma}_{xx}$, transverse shear stress $\bar{\sigma}_{sr}$ and transverse normal stress $\bar{\sigma}_{rr}$ components benefit from a gradual change in volume fraction from the shell's inner surface to its outer surface.

7. Concluding remarks

An analytical linear thermoelasticity solution has been obtained for functionally graded isotropic and orthotropic cylindrical shells that are subjected to steady-state thermal and mechanical loads. The material properties can have an arbitrary variation through the thickness of the shell. A semi-inverse solution is obtained for shells that are simply supported at the edges. The analytically obtained displacements and stresses are compared with those obtained using Flügge and Donnell shell theories for representative isotropic functionally graded shells for a wide range of geometric parameters. We also investigate the advantages of using functionally graded fiber-reinforced composite shells with graded fiber orientations and/or fiber volume fractions over traditional discretely laminated composite shells. Results indicate that the most significant improvements are found in thermal applications due to the reduction in spatial mismatch of thermomechanical material properties. The functionally graded orthotropic shells exhibit smooth

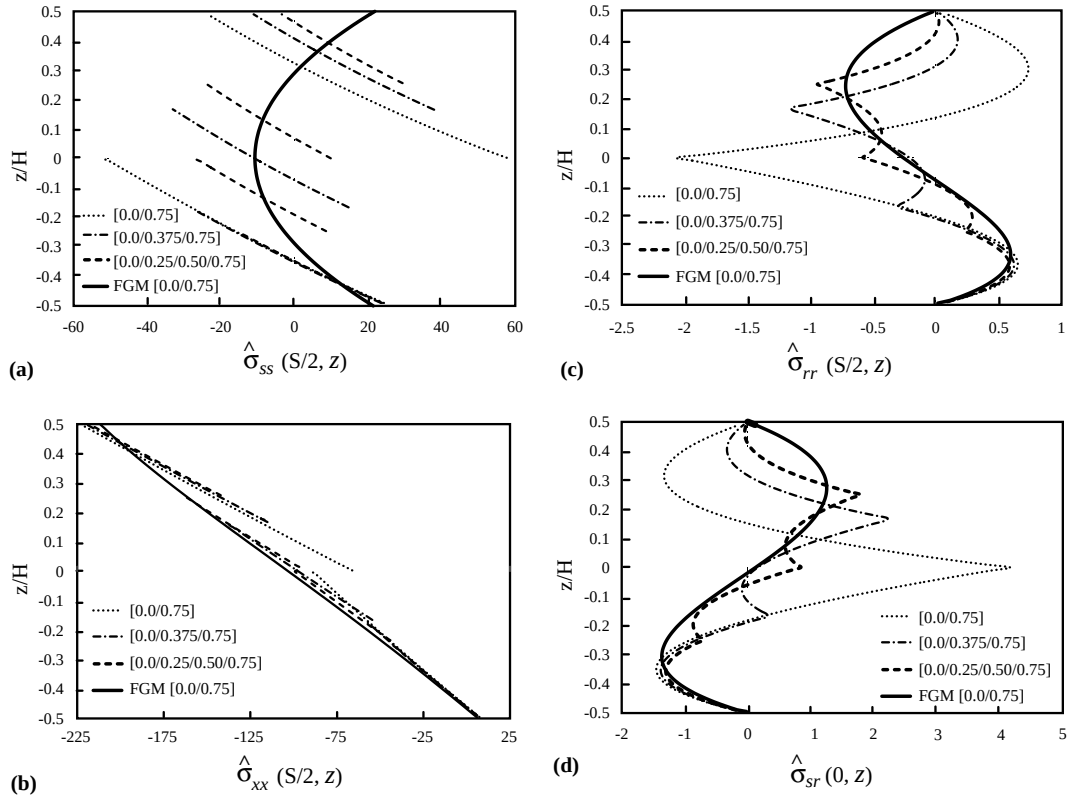

Fig. 11. Effects of graded fiber volume fractions on orthotropic W/Cu cylindrical shells under thermal loading. Shell parameters are $S/H = 5$, $R = 1$ m, $\Theta = \pi/2, \phi_{\mathrm{W}}^{+} = 0, \phi_{\mathrm{W}}^{-} = 0$.

variations of both the in-plane and transverse stress components, thereby minimizing the likelihood of premature failure at an interface between adjoining lamina as in the case of discretely layered fiber-reinforced materials. The ability of the analytical solution to tackle cylindrical shells with arbitrary variations in material properties will enable the designer to tailor the fiber volume fraction and orientation through the thickness of the shell to increase the strength-to-weight ratio or stiffness-to-weight ratio of fiber-reinforced composite shells.

Acknowledgements

This work was supported by a Maine Space Grant graduate fellowship to J.L. Pelletier and the U.S. National Science Foundation through grant DMI-0423485.

References

Cheng, Z.Q., Batra, R.C., 2000. Three-dimensional thermoelastic deformations of a functionally graded elliptic plate. Composites: Part B 31, 97–106.

Donnell, L.H., 1935. Stability of thin walled tubes under torsion. NACA Report 479.

Finot, M., Suresh, S., 1996. Small and large deformation of thick and thin-film multi-layers: effect of layer geometry, plasticity and compositional gradients. Journal of the Mechanics and Physics of Solids 44, 683–721.

Flügge, 1973. Stresses in Shells, second ed. Springer-Verlag, New York.
Hashin, Z., 1979. Analysis of properties of fiber composites with anisotropic constituents. Journal of Applied Mechanics 46, 543–550.
Hill, R., 1965. A self-consistent mechanics of composite materials. Journal of the Mechanics and Physics of Solids 13, 213–222.
Hyer, M.W., Rousseau, C.Q., 1987. Thermally induced stresses and deformations in angle-ply composite tubes. Journal of Composite Materials 21, 454–480.
Loy, C.T., Lam, K.Y., Reddy, J.N., 1999. Vibration of functionally graded cylindrical shells. International Journal of Mechanical Sciences 41, 309–324.
Miracle, D.B., 2001. Aeronautical applications of metal–matrix composites. In: Miracle, D.B., Donaldson, S. (Eds.), ASM Handbook: Volume 21, Composites. ASM International, Material Park, OH, pp. 1043–1049.
Miyamoto, Y., Kaysser, W.A., Rabin, B.H., Kawasaki, A., Ford, R.G., 1999. Functionally Graded Materials: Design, Processing and Applications. Chapman & Hall.
Nowinski, J.L., 1978. Theory of Thermoelasticity with Applications. Sijthoff & Noordhoff International Publishers B.V., Alphen aan den Rijn, Netherlands.
Qian, L.F., Batra, R.C., 2004. Transient thermoelastic deformations of a thick functionally graded plate. Journal of Thermal Stresses 27, 705–740.
Qian, L.F., Batra, R.C., Chen, L.M., 2004. Analysis of cylindrical bending thermoelastic deformations of functionally graded plates by a meshless local Petrov–Galerkin method. Computational Mechanics 33, 263–273.
Reddy, J.N., 2000. Analysis of functionally graded plates. International Journal for Numerical Methods in Engineering 47, 663–684.
Reddy, J.N., 2003. Mechanics of Laminated Composite Plates and Shells: Theory and Analysis, second ed. CRC Press, Boca Raton, FL.
Reddy, J.N., Cheng, Z.Q., 2001. Three-dimensional thermomechanical deformations of functionally graded rectangular plates. European Journal of Mechanics A/Solids 20, 841–855.
Reissner, E., 1945. The effect of transverse shear deformation on the bending of elastic plates. Journal of Applied Mechanics 12, 69–77.
Reiter, T., Dvorak, G.J., Tvergaard, V., 1997. Micromechanical models for graded composite materials. Journal of the Mechanics and Physics of Solids 45, 1281–1302.
Shahsiah, R., Eslami, M.R., 2003. Thermal buckling of functionally graded cylindrical shell. Journal of Thermal Stresses 26, 277–294.
Vel, S.S., Batra, R.C., 2002. Exact thermoelasticity solution for functionally graded thick rectangular plates. AIAA Journal 40, 1421–1433.
Vel, S.S., Batra, R.C., 2003a. Three-dimensional analysis of transient thermal stresses in functionally graded plates. International Journal of Solids and Structures 40, 7181–7196.
Vel, S.S., Batra, R.C., 2003b. Exact thermoelasticity solution for cylindrical bending deformations of functionally graded plates. In: Proceedings of IUTAM Symposium on Dynamics of Advanced Materials and Smart Structures, Yonezawa, Japan, 20–24 May 2002. In: Watanabe, K, Ziegler, F. (Eds.), Dynamics of Advanced Materials and Smart Structures. Kluwer Academic Publishers, Dordrecht.